Structural, Optical and Electrical Properties of Cu-In-O Thin Films Prepared by Plasma-Enhanced CVD

HAO YONGLIANG

(*B. Eng., Wuhan Univ. of Tech., CHINA*)

A THESIS SUBMITTED

FOR THE DEGREE OF MASTER OF SCIENCE

DEPARTMENT OF MATERIALS SCIENCE

NATIONAL UNIVERSITY OF SINGAPORE

2007

Acknowledgements

I would like to use this opportunity to express my sincere gratitude to my supervisor, A/P Gong Hao, for his supervision and help in this project. His guidance and invaluable advice were greatly appreciated.

The help and encouragement I received from Mrs. Liu Ling will always be remembered.

I am appreciative to my group members, Dr.Wang Yue, Dr.Yu Zhigen, Mr.kumar Bhupendra, Mr.Chen Wen, and Mr.Hu Guangxia for their helpful discussions, suggestions and technical assistances.

I would like to thank the technical staff of Department of Material Science and Engineering for their continuous technical support.

Thanks to National University of Singapore for providing scholarship during my tenure as graduate student and for the wonderful studying and working environment without which this work would not have been possible.

Contents

Summary

Indium incorporated/doped copper oxide films may have potential applications in electronic devices. However, the properties of such films were not clear, and this thesis reported a systematic research work on the plasma-enhanced chemical vapor deposition (PE-CVD) preparation and properties of indium incorporated/doped copper oxide films. Copper indium oxide (Cu-In-O) thin films were prepared by PE-CVD using $Cu(acac)_2$ and $In(acac)_3$ precursors with In/Cu atomic ratio of 1 for the first time. The structural, optical and electrical properties of the films prepared at different temperatures and growth conditions were investigated. A structural evolution of the films from amorphous state to nano-grain sized phases was found when the substrate temperature was increased from 400 to 700 °C, and a band structure variation was also observed. An established working hypothesis of double transition metal (TM) oxides could explain the evolution. It is also interesting to find that the band gap can be controlled to vary in a wide range (1.30-1.65 eV) by changing indium concentration in the films, and *p*-type conducting indium incorporated/doped copper oxide was achieved in an In/Cu atomic ratio range of 0.06-0.15, rather than at a zero In/Cu ratio. Various techniques, including Hall

effect, Seebeck effect, X-ray diffraction (XRD), X-ray photoelectron spectroscopy (XPS), scanning electron microscopy (SEM), atomic force microscopy (AFM) and transmission electron microscopy (TEM) were employed in characterizing the samples and understanding the properties of the films.

Key words: Copper indium oxide, CuO:In, Optical property, Electrical property, PE-CVD.

List of Tables

List of Figures

Chapter 1

Introduction

1.1 Problems and Objectives

There is a lack of transparent indium incorporated/doped copper oxide films prepared by chemical vapor deposition (CVD), and their properties are not clear. This work is to perform a systematic study on the CVD growth and gain an understanding of the properties of such films. The objectives of the present work are twofold: first, to understand the crystallographical characteristic of Cu-In-O system under non-equilibrium CVD growth conditions, which is the fundamental of other properties. The other is to study the conduction mechanism and defect structure of indium incorporated/doped CuO thin films.

1.2 Background

Transparent conductive oxides (TCOs) have been widely used for more than 50 years, primarily in the form of impurity-doped single-cation oxide such as In_2O_3 and SnO_2 [1]. Beginning in the 1990s, multi-cation oxides (compound and solid solution) and oxide composites, for example, combinations of binary compounds such as ZnO, CdO, In_2O_3 and SnO_2 have been developed [2, 3]. The multicomponent TCO films can be suitable for various applications because their unique electrical, optical, chemical, and physical properties.

It is noted that almost all of the applicable TCOs are n-type. The lack of available p-type TCOs prevents the fabrication of p-n junctions so that a variety of active functions of TCOs cannot be realized. In 1997, Kawazoe et al. [4] reported the first pulsed laser deposition (PLD) grown p-type conducting $CuAlO_2$, a delafossite TCO, and offered a strategy for identifying p-type conductivity in TCOs. In 2000, our group reported the first CVD grown p-type transparent Cu-Al-O films by plasma-enhanced metal-organic CVD (PE-MOCVD) [5, 6]. More p-type TCO thin films have been fabricated, most of which are in delafossite structure, for example, Cu-Al-O [7], Ag-In-O [8, 9], and Sr-Cu-O [10, 11]. However, the mobilities and carrier concentrations of these films are mostly low, and in most cases the deposited films are insulating. Although relationships among structure, composition, and properties have been studied on these systems in order to explain the underlying mechanism of carrier generation and transportation, the chemical and structural origins of p-type conductivity is still not clear.

For the Cu-In-O system, most of the research in the past decade was associated

with delafossite $CuInO_2$, a runner-up following the prototype of $CuAlO_2$ in the study of delafossite materials due to its bipolar dopability [12]. However, $CuInO_2$ cannot be synthesized directly by solid state reaction and can only be obtained by cation exchange reaction through a complicated process [13], which makes the production of phase-pure $CuInO_2$ difficult [14]. On the other side, research on the multi-cation oxide composites consisted of Cu, In and O elements is rare, particularly for amorphous copper indium oxide thin films. To our best knowledge, there is no report on the preparation of copper indium oxide thin films by PE-CVD.

Cupric oxide, as one of the oldest semiconducting materials, has been studied early for photoconductive applications due to its high solar absorptance and low thermal emittance, however, it has never been adopted for major device applications up to date. The difficulty in controlling its electrical properties is one of the reasons limiting its practical applications. Verwey [15] pointed out that appreciable conductivity could be achieved in the transition metal (TM) oxides only by the introduction of cations of different valency at crystallographically equivalent sites. The substitution of Li ions in CuO leading to the formation of defect structures and/or oxygen deficiency and their effect on the transport properties have been studied [16–19]. However, the effect of doping CuO by column III elements has not been clear, and there is no report of indium incorporated CuO.

Accomplishing the goal of increasing *p*-type conductivity and transparency will require a deeper understanding of the relationships between the structure and the electro-optical properties of these materials. We know that electrical conduction processes are dependent on the composition as well as on the structure of the

sample as prepared. Sample preparation conditions and techniques have therefore a significant role to influence the samples' properties. PE-CVD offers the attraction of *in situ* growth under a variety of atmospheres, the amenability to a large-area coverage with high throughput and conformal coverage, the control of growth chemistry and the possibility of creating metastable structures [1]. The advantages of PE-CVD also include low deposition temperature, high deposition rate, improved adhesion and thermal stability of deposited materials. The low deposition temperature favors the formation of amorphous or nano-structured deposits that often have superior properties [20]. The PE-CVD technique is employed to fabricate Cu-In-O and indium incorporated/doped CuO thin films in this project.

1.3 Thesis Outline

The introduction of this thesis is provided in Chapter 1. A review of p-type TCOs, Cu-In-O system, and copper oxide is presented in Chapter 2. Experimental details of this work are covered in Chapter 3. The structure of Cu-In-O thin films deposited at different experimental conditions and their properties as well are discussed in Chapter 4. The structural, optical, and electrical properties of indium incorporated/doped CuO thin films and their relationships are discussed in detail in Chapter 5. In the final chapter, an overall summary of the current work and suggestions for future work are given.

Chapter 2

Literature Review

Studies of TCO thin films have attracted much attention after World War II, due to their unique combined electrical and optical properties—low absorption of visible light, high electrical conductivity, and high carrier mobility. The list of potential TCOs has expanded to include, for example, impurity-doped ZnO, $GdInO_x$, SnO_2, tin-doped indium oxide (ITO), and many others. These materials have found specific uses in various fields such as display devices, low emissive and electrochromic windows, thin film photovoltaic (PV) devices, heated windscreen for cars, defrosting widows, oven widows, static dissipation, touch panel screens, etc [21–28]. However, all of applicable TCOs are n-type semiconductors, and the lack of available p-type TCO limits potential applications of TCO materials.

In this chapter, some p-type TCOs are introduced in Section 2.1, from which we may understand why the study of p-type TCOs has been one of the most exciting research areas and where the difficulties lie in realizing p-type TCOs. In Section

2.2, a review on Cu-In-O system is focused on. In Section 2.3, a review of studies on copper oxide is given, especially on doped CuO thin films, which is the focus of this project.

2.1 P-type TCOs

A few p-type TCOs, including NiO, ZnO, delafossite TCOs and CuO, have been studied. With a band gap of 3.6-4.0 eV [29], NiO is a candidate for *p*-type TCO films. NiO is susceptible to non-stoichiometry, and this may give rise to semi-conductive properties and strong optical absorptions, the latter results in poor transparency. Saito et al. [30] obtained semi-transparent conducting *p*-type NiO thin films with a conductivity of 7.14 $S{\cdot}cm^{-1}$ and a hole concentration of $1.3{\times}10^{19}$ cm^{-3} by magnetron sputtering. The conduction mechanism in NiO [31, 32] is still questionable.

ZnO has come to the forefront in the past decade because of an increasing need for short-wavelength photonic devices and high-power, high-frequency electronic devices [33]. ZnO is basically *n*-type in character, although there is still controversy as to what are the relevant native defects of this oxide [34]. Weak *p*-type conduction in ZnO thin films were reported by several groups [35–38] in recent years. Since ZnO is not the focus of this thesis, more details are not presented.

In 1997, Kawazoe et al. [4] reported a PLD prepared *p*-type delafossite $CuAlO_2$. Our group then reported the first PE-CVD grown *p*-type Cu-Al-O films according to the review paper of Banerjee and Chattopadhyay [5,6]. After the $CuAlO_2$, other

p-type copper based oxide films with inclusion of Ga, Sc, In and Y [12,39–42] have been reported. However, no CVD growth of these films has been found, and the reported methods involved high deposition temperature (above 700 °C) limiting their application in multilayered structures. Finding a more efficient route to synthesis *p*-type oxide thin films requires more work on chemical and structural research of these ternary systems.

In the process of exploring *p*-type TCO compounds, new TCO materials consisted of multicomponent oxides have been developed. Minami and his coworkers [8] prepared amorphous In_2O_3-Ag_2O thin films by conventional RF magnetron sputtering. After post-annealing, the films with Ag_2O contents of 40-60 wt% exhibited *p*-type conduction. Although these films showed relatively high conductivities (10-100 $S{\cdot}cm^{-1}$), they are not transparent, with the average transmittance in the visible range of about 20%. Asbalter and Subrahmanyam [43] prepared polycrystalline In_2O_3-Ag_2O thin films by reactive electron beam evaporation technique, however, with poor conductivities and low transparencies. *P*-type strontium-copper mixed oxides films with transparency of over 60% in the visible range and conductivity as high as $5.3{\times}10^{-2}$ S/cm were prepared by e-beam evaporation [10]. The films consist of CuO, Cu_2O, and $SrCu_2O_2$ phases. *P*-type transparent Cu-Al-O thin films containing nanocrystalline phases of $CuAlO_2$ and Cu_2O were prepared by PE-MOCVD [5]. A conductivity of 2 S/cm and optical band gap of 3.75 eV were achieved. Co-doping theory [44] was applied to explain the high conductivity of the films. Our group [7] reported that Cu-Al-O films produced by using reactive co-sputtering of metallic Cu and Al targets are conducting at lower Al content but behave like to be insulating at higher Al content.

2.2 Copper Indium Oxide System

Of the newly found Cu-based delafossite TCOs, $CuInO_2$ has been proven [12, 45] to be of bipolar dopability, the capability of being doped to be both *p*-type (with Ca) and *n*-type (with Sn). The interesting phenomena were explained through the "doping limit rule" [46], that a relatively low conduction band minimum (CBM) and high valence band maximum (VBM) observed in $CuInO_2$ implies good *n*- and *p*-type dopability.

No phases have been reported in the Cu-In-O system expect $Cu_2In_2O_5$ [47] and $CuInO_2$ [13]. $Cu_2In_2O_5$ can be synthesized by solid state reaction of CuO and In_2O_3 at 950 °C in air for a few days with several intermediate regrinding processes [48]. Cu-In-O films deposited from a sintered $Cu_2In_2O_5$ target by using a pulsed laser deposition (PLD) method can be transformed into $CuInS_2$ films in H_2S gas, which has been a popular method to prepared polycrystalline $CuInS_2$ thin films as a possible material for photovoltaic devices [49]. Using this method, Wada and his coworkers reported [49] that the Cu-In-O film deposited at the substrate temperature of 600 °C was a mixture of In_2O_3 and CuO.

By calculating the reaction enthalpy of Cu_2O, In_2O_3, and $CuInO_2$, Liu [50] reported that the formation energy of the ternary compound $CuInO_2$ is 0.056 eV higher than that of Cu_2O and In_2O_3. In other words, fabrication of ternary $CuInO_2$ from the parent elements is no more energetically economy than that of the end-point binary compounds Cu_2O and In_2O_3. The result is consistent with the fact that it is difficult to fabricate $CuInO_2$ by solid state reactions with the end-point binary compounds in Shimode's [13] and Hahn's [51] studies. In Shimode's study,

solid state reaction occurred neither in the Cu_2O-In_2O_3 nor in the Cu_2O-$In(OH)_3$ system at 1200 °C for 24 hours in Argon. As to our best knowledge, there is no Cu-In-O equilibrium phase diagram reported up to date.

$CuInO_2$ is often produced through an ion-exchange reaction method with the alkali ternary compounds like $LiInO_2$ or $NaInO_2$ as follows:

$$CuCl + NaInO_2 \longrightarrow CuInO_2 + NaCl. \tag{2.1}$$

However, residual Cu_2O and In_2O_3 were also observed in the substitution reaction products, although the temperature of the reaction was not beyond the decomposition point of $CuInO_2$, i.e., 600 °C [13]. Despite recent progress in improving the yield of this reaction [52], producing phase-pure $CuInO_2$ is difficult.

In 2004, Teplin et al. [53] reported the growth of phase pure $CuInO_2$ thin films from both undoped and Ca-doped $Cu_2In_2O_5$ targets by PLD. XRD spectra of films deposited from the undoped target showed that phase pure $CuInO_2$ films could be obtained over a temperature range of 400-600 °C at an oxygen partial pressure of 7.5 mT. Films grown in a more oxidizing 15 mT O_2 are $Cu_2In_2O_5$ and films grown in a more reducing Ar show only In_2O_3 in the XRD spectra.

2.3 Copper Oxides

Copper oxides have been studied as semiconductor materials for a long time because of their following advantages: non-toxic nature, abundance of starting material (Cu), cheap production processing, and reasonably good electrical and optical properties [54].

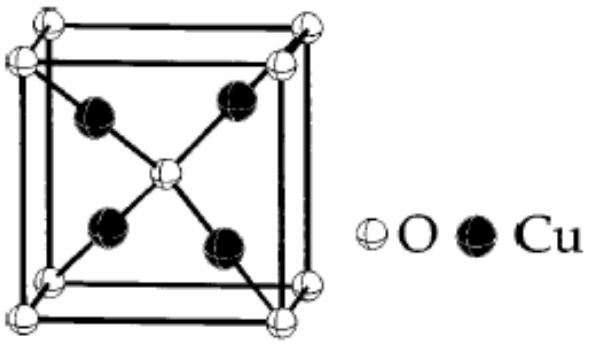

Figure 2.1: Cubic crystal structure of Cu_2O. (Adapted from E. Ruiz, S. Alvarez, P. Alemany and R.A. Evarestov, Physical Review B 56, 7189 (1997))

Cuprous oxide (Cu_2O), a *p*-type semiconductor with a direct band gap of 2.0 eV [55], is one of the materials feasible for fabricating of thin film solar cells due to its high absorption coefficient in the visible range and large hall mobility (usually > 10 cm^2/Vs) [56]. Cu_2O crystallizes in the cuprite structure, formed by a bcc array of oxygen atoms with metal atoms inserted between two consecutive oxygen layers, in such a way that each oxygen atom is surrounded by a tetrahedron of copper atoms. Each copper atom is coordinated to two oxygen atoms, forming linear CuO_2 units, as shown in Fig. 2.1.

Properties of Cu_2O films depend very much on their method of preparation and practical applications have not been achieved to date because of the difficulty

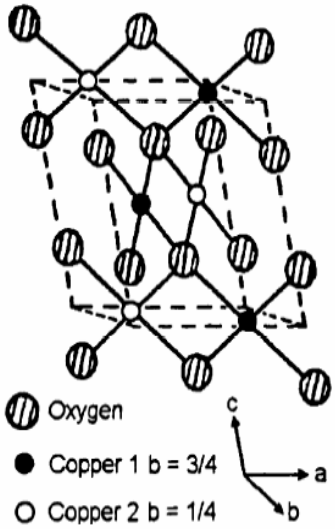

Figure 2.2: Monoclinic crystal structure of CuO. (Adapted from B.X. Yang, T.R. Thurston, J.M. Tranquada and G. Shirane, Physical Review B 39, 4343 (1989))

in controlling the electrical and optical properties. For controlling the electrical properties, the selection of proper dopant for Cu_2O is a key point. It has been reported that N, Cl, Si, Cd, and In are effective p-type dopant elements [57–60], and the lowest resistivity of 9 Ωcm was obtained in the case of Cd-doped bulk Cu_2O [59].

CuO, a p-type semiconductor with an indirect band gap of 1.0-1.9 eV [55, 61–65], has attracted a considerable attention in the past two decades due to its fundamental importance in understanding materials properties such as high-temperature superconductivity and its practical or potential applications in photothermal and photoconductive devices [54, 66], gas sensing [67, 68], magnetic storage media [69], solar cells [61, 70], and spintronic devices [71, 72] .

CuO has a monoclinic structure, in which Cu atoms are coordinated to four coplanar oxygen atoms situated at the corners of an almost rectangular paral-

lelogram, as showed in Fig. 2.2. Theoretically, a correct electronic density of states of CuO, a special Mott insulator having a strong electron-electron interactions, has been achieved by the first-principles calculations using the LSDA+U method [73, 74]. However, the detailed band structure of CuO have not yet been obtained by this method so far. Wu and his co-workers reported that CuO is intrinsically a p-type semiconductor because Cu vacancies are the most stable defects in both Cu-rich and O-rich environments by using the same approach [64].

Several techniques have been employed to prepare CuO films, such as chemical vapor deposition (CVD) [75–78], thermal oxidation of copper [79], dip-coating [80], sputtering [81–83], electrochemical deposition [84], and pulsed laser deposition [85]. Many properties of CuO thin films are associated with the small grain size or amorphous structure [86], which are strongly dependent on the method of preparation. For example, pure CuO with good stoichiometry is almost insulating, however large variations in resistivity (1-10^7 Ωcm) [76] were reported.

It has been reported that Li or Na are effective as p-type dopant for CuO [16–19] which can be explained by the reaction as,

$$Li_2O + \frac{1}{2}O_2 \rightarrow 2Li'_{Cu} + 2O^*_O + 2h^{\cdot}, \tag{2.2}$$

where a hole generates to compensate the negative charge of Li substituted for CuO. A problem for Li-doped CuO is that impurity phases such as Li_2CuO_2, $LiCu_2O_2$ and $LiCu_3O_2$ will form at different Li concentrations [17, 19].

The effect of doping CuO by column III elements has not been clear. Al_2O_3 doping into CuO was shown to reduce the hole conductivity of CuO [16, 18, 87]. However, Suda et al. [18] observed a higher conductivity than that of pure CuO in the bulk CuO containing 0.1at% Al_2O_3 and the chemisorbed oxygen in the porous sample was considered as a possible explanation. No CuO incorporated with indium, another column III element, has been reported, to the best of our knowledge. The increase of p-type conductivity by column III elements incorporation may appear strange, as the substitution of Cu by a group III element (such as In or Al) should lead to a reduction in net hole concentration and a decrease in conductivity. To alleviate the ambiguities, indium incorporated/doped CuO thin films will be investigated in this work.

Chapter 3

Experimental Details

The thin film deposition equipment and growth process are presented in this chapter. Also provided are outlines of the experimental techniques used for the structural, compositional, optical and electrical characterizations. Section 3.1 describes the equipment used for thin film deposition and the thin film growth process. Section 3.2 presents background information of characterization techniques used in this project.

3.1 Thin Film Deposition Equipment and Process

In the present work, all the copper indium oxide thin films were deposited by a home-built plasma-enhanced chemical vapor deposition (PE-CVD) system. Although the exact arrangement of a CVD apparatus varies widely depending on the particular applications, generally, two main components are embodied: the transportation system and the reaction system.

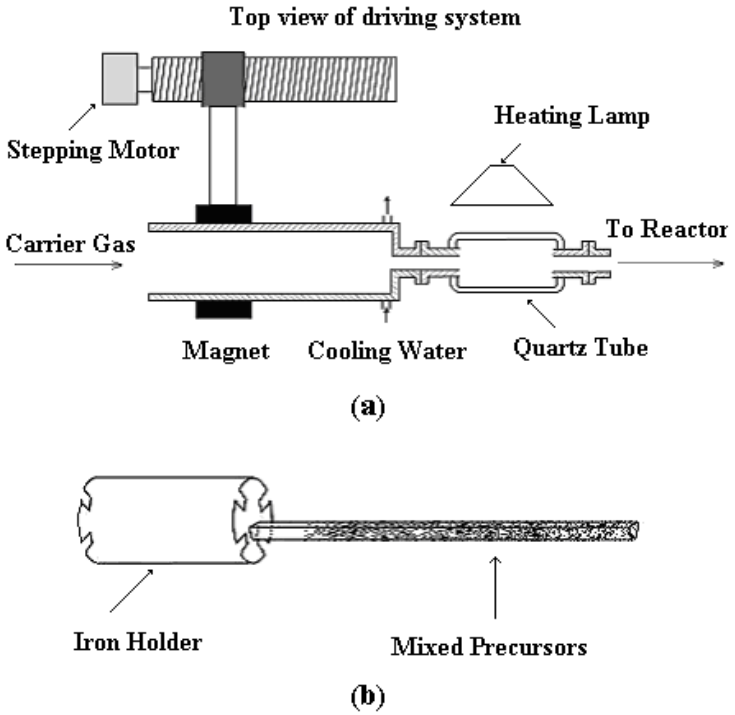

Figure 3.1: Schematic diagrams of (a) transportation system and (b) precursor transportation boat.

The transportation system is in charge of both the transport of precursor into the reaction chamber and the control of carrier and reactive gas flow rate. Its design depends on the source compounds. In the present system (see Fig. 3.1(a)), metal-organic precursors in solid state are employed. The mixed precursors in a quartz coat (see Fig. 3.1(b)) are transported to the heating region, sublimated by

being heated with a halogen lamp and then carried by argon gas to the reactor. This heating region is equipped with a quartz tube and a halogen lamp. The infrared radiation from the lamp through the quartz tube causes the sublimation of the precursors. The external wall of the quartz tube is kept around 200 °C. The sublimed precursors carried by argon gas are driven into the reaction chamber after mixing with oxygen, the reactive gas. In Fig. 3.1(b), it can be seen that the quartz boat is fixed with an iron holder, which can be attracted by a magnet and the magnet is driven by a stepping motor.

The reaction system is the heart of a PE-CVD setup. In general, a PE-CVD reactor has several integrants: a vacuum chamber with pumping system to maintain reduced pressure, a power supply to create the discharge, and a temperature control system.

Four basic reactor configurations are normally used in PE-CVD setups: capacitively coupled, inductively coupled with substrates downstream of the discharge, inductively coupled with substrates within the glow region, and electron cyclotron resonance configuration. In the present system, the capacitively coupled mode is used. The plasma currently used in CVD is glow-discharge plasma [88], which is generated in a gas by a high-frequency electric field, such as microwave (2.45 GHz), at a relatively low pressure. In such a plasma, the following events occur: in a high-frequency electric field, the gases are ionized to form electrons and ions; the electrons, with their extremely small mass, are quickly accelerated to high velocity [20]; the heavier ions with their much greater inertia cannot respond to the rapid changes in field direction so their velocities remain low, as opposed to the

electron velocity. The high-energy electrons collide with the gas molecules resulting in dissociation and generation of reactive chemical species and the initiation of the chemical reactions. The most common frequencies used for CVD are the microwave at 2.45 GHz and radio frequency (RF) at 13.56 MHz [88], and our system adopted the later. A schematic diagram of the reactor used in the current work is shown in Fig. 3.2.

The reaction chamber is of round shape and made of stainless steel. A pump system with a rotary pump as the fore-pump and a turbo-molecular pump keeps the base pressure of the chamber at around 5×10^{-6} Torr. Inside the chamber, a ceramic heater (SG Control Engineering Pte. Ltd.) is used to heat up the substrates. The temperature of the heater is up to 800 °C.

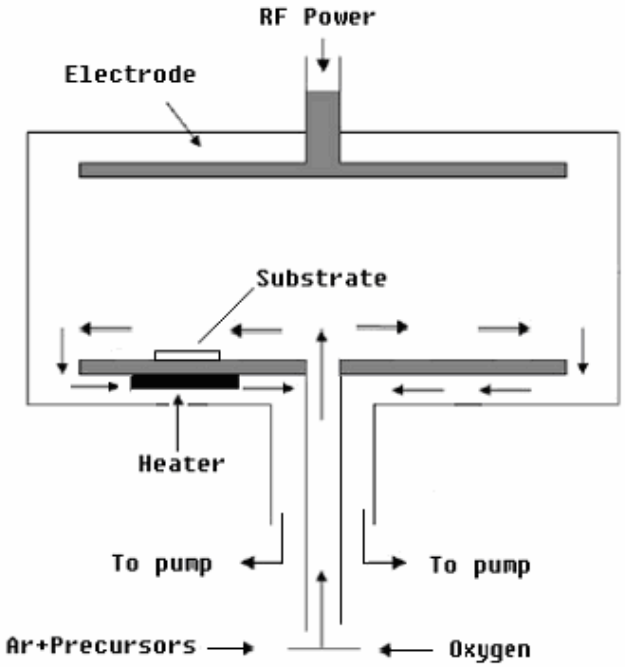

Figure 3.2: Schematic diagram of the reactor of the PE-CVD system employed in this project.

Metal-organic $Cu(acac)_2$ (copper acetylacetonate, ACRO 99%)and $In(acac)_3$ (indium acetylacetonate, ALDRICH 99.99%) were used as precursors for this project due to their low sublimation temperatures and high volatility. Their 2-dimensional structures are shown in Fig. 3.3.

Quartz plates of dimension 10×10 mm^2 and (100) silicon were employed as substrates. Before being introduced into the reaction chamber, the substrates were ultrasonically cleaned by ethanol and acetone, washed by deionized water, and then blown dry by nitrogen. Prior to the deposition, the substrates were heated at 400 °C for degassing. The deposition atmosphere was maintained during cooling to room temperature.

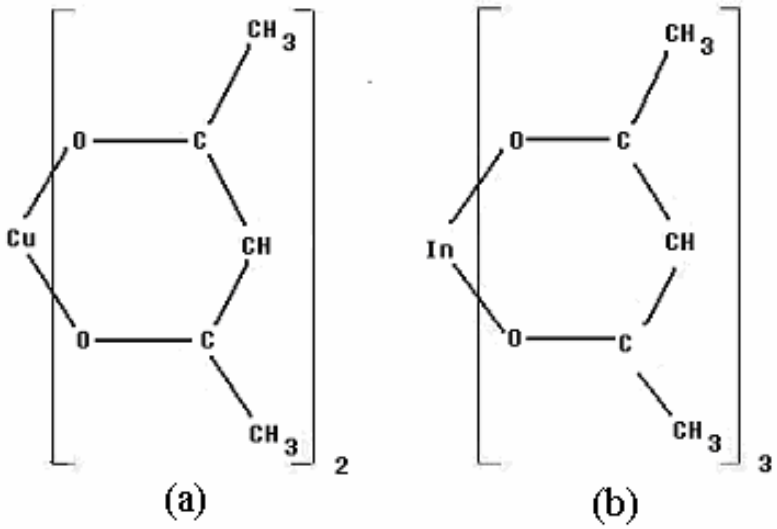

Figure 3.3: Structures of (a) copper and (b) indium acetylacetonate precursors.

3.2 Characterization Techniques

3.2.1 X-ray diffraction (XRD)

X-ray diffraction (XRD) is a versatile, non-destructive analytical technique for identification of the phases in materials. The measurement results provide direct information of spacings of crystal planes of a sample.

An incident monochromatic X-ray impinging on a sample is diffracted if the X-ray beams are scattered by adjacent crystal planes are in phase (constructive interference) according to the Bragg's equation [89]:

$$2d \sin\theta = n\lambda \tag{3.1}$$

where λ is the wavelength of the X-ray source, θ is the angle of scattering (Bragg angle), d is the lattice spacing between adjacent crystal planes, and n is an integer that represents the order of diffraction.For crystalline materials, characteristic diffraction peaks are obtained. Each peak represents diffraction of the X-ray beam by a set of parallel crystal planes *(hkl)*. For amorphous materials, a broad diffused pattern is obtained due to the inherent short-range order.

In addition, the diffraction peak intensity can be a qualitative measure of the degree of texturing; that is, the intensity increases with the fraction of crystallites in the sample which have that atomic plane parallel to the surface. The width of the peak $\Delta(2\theta)$(in radians), at half of its maximum intensity is a measure of the size of the crystal grains. This is because a larger stack of planes contributing to

destructive interference at "off-Bragg" angles results in a sharper Bragg peak, as described by Scherrer's formula [90]:

$$G = \frac{0.9\lambda}{\Delta(2\theta)\cos\theta} \tag{3.2}$$

when the grains are larger than the film thickness h, $G = h$; when they are smaller, the grain size G can be estimated from the above equation.

In a case where stress may be present, a more rigorous method involving several diffraction peaks is required. Therefore, Scherrer's formula should be used only as a rough guide for particle/grain size. To characterize thin film samples with XRD, grazing incidence mode (a small grazing angle of incidence) should be employed because the penetrating power of X-ray is so great that with typical incident angles the resulted path length through films would be too short to produce diffracted beams of sufficient intensity. This means that the optics of the thin film diffractometer is not symmetrical in this application.

A Bruker D8 Advance X-ray diffractometer (Cu-K_α 1.5406 Å) was used to characterize all the thin film samples with the fixed incidence angle of 1° and step size of 0.02°.

3.2.2 Energy dispersive X-ray spectrometry

Energy dispersive X-ray (EDX) analyzer is ubiquitously attached to scanning electron microscope (SEM) and transmittance electron microscope (TEM) for chemical analysis. When a high energy electron beam hits the specimen under investigation,

some of electrons are dislodged, thus ionizing atoms of the specimen. In this state atoms are unstable and to reach a stale state, outer cell electrons quickly fill the vacancies created by secondary electrons. In this neutralization process, an X-ray with an energy characteristic of the parent atom is emitted. By collecting and analyzing the energy of these X-rays, the constituent elements of the specimen can be determined.

In the present work, EDX attached to a Philips XLSERIE XL30/FEG field emission gun SEM is used for elemental analysis. The energy of the electron beam typically in the range of 5-20 KeV has been used for analysis. The working distance between sample and the electron gun was kept at 10 nm. The Counter Per Second (CPS) and DT was maintained in the range of 1000-2000 and 25-40, respectively, by adjusting voltage and spot size for accurate results.

3.2.3 UV-visible spectroscopy

UV-visible spectrophotometry involves the measurement of light transmission and absorption of a sample with wavelengths in the near ultraviolet (UV) region (200-400 nm), the visible region (400-700 nm), and the near infrared (IR) region (700-1100 nm). For a double beam spectrophotometer, the operation principle is that a light beam from a tungsten-halogen lamp or a deuterium lamp (depending on the wavelength) is separated into its component wavelengths by a prism or diffraction grating. Each monochromatic beam in turn then splits into two equal intensity beams by a half-mirrored device. One beam, the sample beam, passes through the thin film sample under investigation. The other beam, the reference beam,

passes through a reference substrate. The intensities of these light beams are then measured by electronic detectors. Over a period of time, the spectrophotometer automatically scans all the component wavelengths in the manner descried. Upon testing, the spectrum of all the components in the system in the absence of sample was measured firstly to determining the baseline. The intensity of the baseline, together with the intensity of the reference beam, which should have suffered little light absorption, are subtracted from the intensity of the sample beam. Thus, the final absorption spectrum is only resulted from the absorption of light by the tested sample itself.

In the current work, Shimadzu UV-1601 UV-visible spectrophotometer was used for the measurement. The medium scanning mode (with a sampling interval of 0.5 nm) and a slit width of 2.0 nm were used for the measurement.

3.2.4 X-ray photoelectron spectroscopy (XPS)

Surface analysis by XPS [91] involves irradiating a solid in vacuum with monoenergetic soft X-rays and analyzing the emitted electrons by energy. The spectrum is obtained as a plot of the number of detected electrons per energy interval versus their kinetic/binding energy. Each element has a unique XPS spectrum due to characteristic binding energy of its core electrons. Because the mean free path of electrons in a solid is very small, the detected electrons originate only from the top few atomic layers, making XPS a unique surface-sensitive technique for chemical analysis. Quantitative or semi-quantitative data can be obtained from peak heights or peak areas, and the identification of chemical states can often be made

from the measurement of the exact positions and separations of peaks, as well as from certain spectral features.

When photons interact with atoms, they cause electrons in the surface region to be emitted by the photoelectric effect. The kinetic energy (KE) of an emitted electron is related to the other material properties as follows

$$KE = h\nu - BE - \Phi_s \tag{3.3}$$

where $h\nu$ is the energy of the photon, BE is the binding energy of the atomic orbital from which the electron originates referring to Fermi level, and Φ_s is the spectrometer work function. The binding energy may be regarded as the energy difference between the initial and final energy states as the photoelectron leaves the atom. Because there are a variety of possible final states of the electrons from each type of atom, there are a corresponding variety of kinetic energies of the emitted electrons. Moreover, there is a different probability or cross-section for each final state. Because each element has a unique set of binding energies, XPS can be used to identify and determine the concentration of the elements in the surface. Variations in the elemental binding energies (the chemical shifts) arise from the differences in the chemical potential and polarizability of the compounds. These chemical shifts can be used to identify the chemical state of the material being analyzed.

In the present work, XPS analysis of the films was carried out by using a PHI Quantera Scanning X-Ray Microprobe with Al Kα (1486.6 eV) X-ray source and spot size of 200 μm.

3.2.5 Transmission electron microscopy (TEM)

Transmission electron microscopy (TEM) is an imaging technique whereby a beam of electrons is focused onto a specimen causing an enlarged version to appear on a fluorescent screen or layer of photographic film, or to be detected by a CCD camera. Like all matter, electrons have both wave and particle properties (as theorized by Louis-Victor de Broglie), and their wave-like properties mean that a beam of electrons can in some circumstances be made to behave like a beam of radiation. The wavelength is dependent on their energy, and so can be tuned by adjustment of accelerating fields, and can be much smaller than that of light, yet they can still interact with the sample due to their electrical charge. Electrons are generated by a process known as thermionic discharge in the same manner as the cathode in a cathode ray tube, or by field emission; they are then accelerated by an electric field and focused by electrical and magnetic fields onto the sample. The electrons can be focused onto the sample providing a resolution far better than is possible with light microscopes, and with improved depth of vision.

A crystalline material interacts with the electron beam mostly by diffraction rather than absorption. The intensity of the diffraction depends on the orientation of the planes of atoms in a crystal relative to the electron beam at certain angles the electron beam is diffracted strongly, sending electrons away from the axis of the incoming beam, while at other angles the beam is largely transmitted. Specimen holders allow the user to tilt the specimen to a range of angles in order to obtain specific diffraction conditions, and apertures placed below the specimen allow the user to select electrons diffracted in a particular direction. A high con-

trast image can therefore be formed by blocking electrons deflected away from the optical axis of the microscope by placing the aperture to allow only unscattered electrons through. This produces a variation in the electron intensity that reveals information on the crystal structure. In the most powerful diffraction contrast TEM instruments, crystal structure can also be investigated by High Resolution Transmission Electron Microscopy (HRTEM), also known as phase contrast imaging as the images are formed due to differences in phase of electron waves scattered through a thin specimen. In the present study, a TEM (JEOL2020F) operated at 200 KeV was used.

3.2.6 Atomic force microscope (AFM)

An atomic force microscope (AFM) can provide pictures of surfaces such as roughness, particle size, etc. The AFM works by scanning a very sharp tip over a surface much the same way as a phonograph needle scans a record. The tip is positioned at the end of a cantilever beam shaped much like a diving board. As the tip is repelled by or attracted to the surface, the cantilever beam deflects. The magnitude of the deflection is captured by a laser that reflects at an oblique angle from the very end of the cantilever. A plot of the laser deflection versus tip position on the sample surface provides the resolution of the hills and valleys that constitute the topography of the surface. The AFM can work with the tip touching the sample (contact mode), or the tip tapping across the surface (tapping mode) much like the cane of a blind person. A Digital Instrument NanoScope IIIa Scanning Probe Microscope was used to investigate the surface by using the software attached with

the instrument, NanoScope III, Version 5.12r3. The tapping mode AFM is used for surface imaging and roughness measurement of the films.

3.2.7 Hall effect and electrical testing equipment

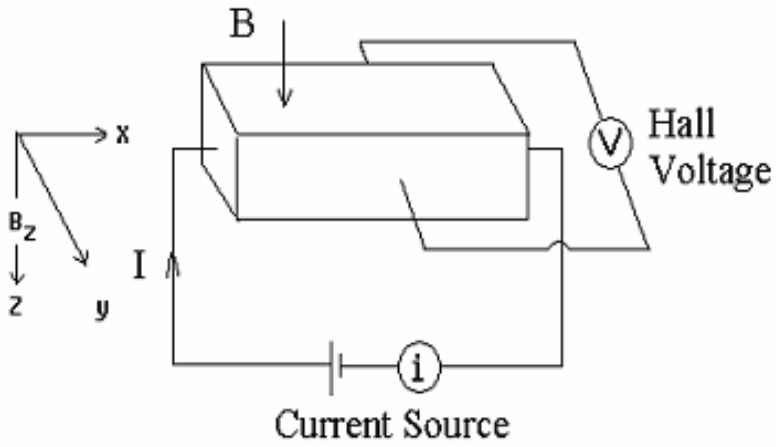

Figure 3.4: Schematic setup for Hall Effect measurement.

The Hall Effect is based on the deflection of charge carriers under the influence of perpendicular magnetic field [92]. Consider a sample in the form of a rectangular bar as shown in Fig. 3.4. An electric field E is applied in the x-direction while a magnetic field B is applied along the z-direction. According to Lorentz's law, the force acting on the charged particle will then follow F=q(v×B), where v is the velocity of the particle and q is its charge. The Lorentz force F is thus a vector perpendicular to both v and B in a right-handed direction (i.e., in the y-direction for this case). Hence, free charge carriers will be deflected to the same side, resulting in a separation of charge across the two opposite sample surfaces perpendicular to the y-axis [93]. An electric field, E_H, called the Hall field, is thus created across these sample surfaces.

The Hall field may be expressed in terms of the current density J as

$$E_H = R_H JB \tag{3.4}$$

where R_H is defined as the Hall coefficient, which is related to the density of charge carriers, N, by

$$R_H = \frac{1}{Ne} \tag{3.5}$$

The sign of R_H depends on the sign of the charge, and is negative for electrons and positive for holes.

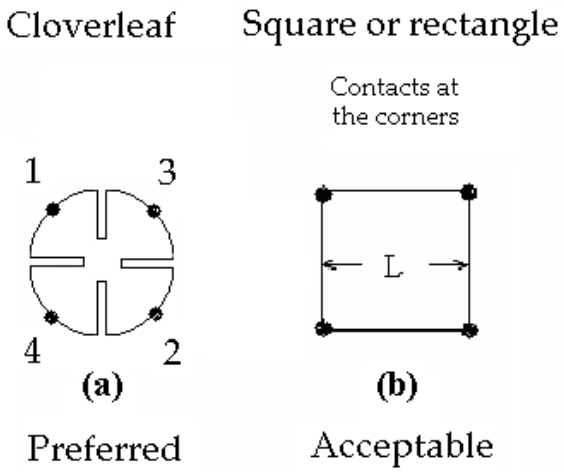

Figure 3.5: Preferred (a) and acceptable (b) geometries for Hall Effect measurement in the Van der Pauw configuration.

Van der Pauw developed the Hall Effect measurement of thin film samples [93]. Two common geometries for a thin sample are shown in Fig. 3.5. To minimize the error in the measurement of the Hall voltage (as current flow may not be perpendicular to the line joining contacts 1 and 2), both the voltage with the magnetic field $V_{12}(\pm B)$ and without the magnetic field $V_{12}(0)$ are usually measured. Van

der Pauw showed that the Hall coefficient is given by

$$R_H = \frac{[V_{12}(B) - V_{12}(0)]d}{I_{34}B} = \frac{[V_{12}(B) - V_{12}(-B)]d}{2I_{34}B} \tag{3.6}$$

where d is the thickness of the film, B is the magnetic field and I_{34} is the current flowing from contact 3 to contact 4.

The sample resistivity can also be measured with the Van der Pauw method. In this case two adjacent contacts such as 2 and 3 (I_{23}) are used as current contacts while the two remaining contacts are used for measuring the voltage drop (V_{41}). The resulting resistance is defined as $R_{41,23}$

$$R_{41,23} = |V_{41}|/I_{23} \tag{3.7}$$

Another measurement is further made, in which the current is sent through contacts 1 and 3 (I_{13}) instead while the voltage is measured across contacts 2 and 4 (V_{24}). From the resulting resistance $R_{24,13}$, together with the previously obtained $R_{41,23}$, can be calculated with the expression,

$$\rho = \frac{(R_{24,13} + R_{41,23})f}{2\ln 2} \tag{3.8}$$

where f is a factor that depends on the ratio $R_{24,13}/R_{41,23}$ and f is equal to 1 when the ratio is exactly 1 and decreases to 0.7 when the ratio is 10. Usually a large value for this ratio is undesirable, and $R_{24,13}/R_{41,23}$ is kept nearly 1 in this work.

Resistivity, carrier concentration, and mobility of all the films were measured

with a BIO-RAD's HL 55WL Hall system in a Van der Pauw configuration (the acceptable geometry). Sputtered gold was used for the contact.

Chapter 4

Cu-In-O Thin Films

With the aim of understanding the Cu-In-O ternary system prepared by PE-CVD, a systematic study of Cu-In-O thin films is reported in this chapter. The crystallographical characteristic and phase composition of the Cu-In-O thin films prepared by PE-CVD using precursors $Cu(acac)_2$ and $In(acac)_3$ with In/Cu atomic ratio (M ratio) of 1 were investigated. Section 4.1 reports structural properties of the films with respect to the influence of substrate temperature and growth atmospheres. Section 4.2 outlines the optical and electrical properties of the films. A summary of this chapter is given in Section 4.3.

4.1 Structural Properties

4.1.1 Effect of growth temperature

Cu-In-O films were deposited on x-cut quartz and (100) silicon substrates under the following conditions: O_2 flow rate at 15 sccm, Ar flow rate at 15 sccm, plasma power at 150 W, and working pressure at 8 Pa. The substrate temperatures during the growth process were 400, 500, 600, and 700 °C, respectively. Fig. 4.1 shows the XRD spectra of the films.

The films prepared on x-cut quartz substrates will be discussed first. As shown in Fig. 4.1 (a), there was a hump at 33.1° for the film deposited at 400 °C and a hump at 32.5° for the 500 °C film, respectively. These humps are too wide (full width at half maximum, FWHM, $\sim 4.5°$) to be explained as a crystalline structure, i.e., these films are amorphous. When the substrate temperature increased to 600 °C, three peaks at 30.83°, 32.19° and 32.98°, and a few small humps were observed. For the film prepared at 700 °C, there were three sharper peaks at 30.94°, 33.08° and 32.32°, indicating that a stronger crystallization occurred at a higher substrate temperature. The average grain size calculated by the Scherrer formula (Eq. 3.2) using the peak at 33.08° was estimated to be around 19 nm. It should be pointed out that the Scherrers formula could only be used as a rough guide to the crystallite size in the sample, since other broadening effects such as strain and instrument broadening might also be present.

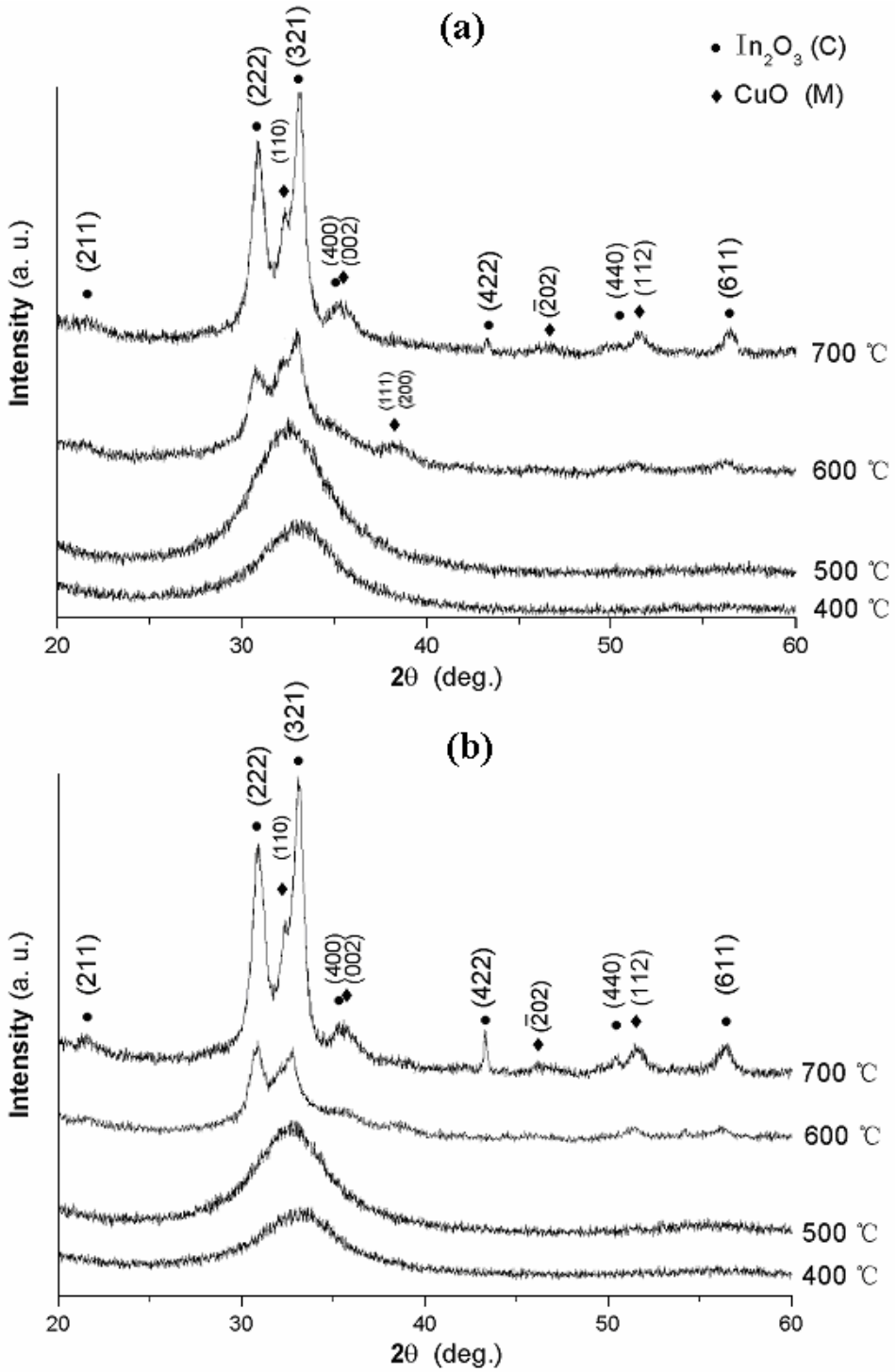

Figure 4.1: XRD spectra of Cu-In-O films prepared on (a) x-cut quartz and (b) (100) silicon substrates at different temperatures: 400, 500, 600, and 700 °C. C and M denote cubic and monoclinic, respectively.

For the films prepared on (100) silicon substrates at the same temperatures, their XRD spectra shown in Fig. 4.1 (b) are similar to those in Fig. 4.1 (a), indicating that the structures of the films prepared at the above-mentioned conditions are less dependent of substrate materials.

29 Cu 63.54	30 Zn 65.37	31 Ga 69.72	32 Ge 72.59	33 As 74.92
47 Ag 107.87	48 Cd 112.40	49 In 114.82	50 Sn 118.69	51 Sb 121.75
79 Au 196.97	80 Hg 200.59	81 Tl 204.37	82 Pb 207.19	83 Bi 208.98

Figure 4.2: A group of heavy metal elements with (n-1)d^{10}ns^0 electronic configuration in the Periodic Table.

It is important to point out that In_2O_3 films prepared by CVD technique using $In(acac)_3$ and oxygen at deposition temperature as low as of 350 °C are still polycrystalline [94], and polycrystalline CuO films prepared at even 280 °C by an atmospheric-pressure chemical vapor deposition method were reported [78]. However, when the mixed precursors were used, our films deposited at below 500 °C were still amorphous. Even at 600 °C, only small nano-grains were observed in the films. These results are well consistent with Hosono's argument that double transition metal (TM) oxides are preferable to monoxide with respect to the formation of an amorphous state [95]. According to his working hypothesis, overlap of ns orbital of heavy metal cations (HMCs) having (n-1)d^{10}ns^0 electronic structure is large due to spherical symmetry and insensitive to any angular variations in the M-O-M bonds (where M is a metal cation) compared with *p-p* or *d-p* or-

bitals having high anisotropy in geometry. It is well known that the bottom part of the conduction band in these oxides is primarily composed of ns orbitals of HMCs [96]. Three novel transparent electronic conducting amorphous semiconductors were developed following this hypothesis [95]. Notably, Cu and In are two of fifteen elements having stable cations with (n-1)d^{10}ns^0 configuration in the periodic table (see Fig. 4.2) The validity of this hypothesis will be further verified by the work introduced in Chapter 5, and its significance to the possibility of preparation of delafossite $CuInO_2$ by PE-CVD will be discussed later.

In order to identify phases in the films, the XRD spectrum of the film deposited on (100) silicon substrate at 700 °C, as a representative sample, will be discussed in detail. In the spectrum, there were four peaks at 30.93° (2.889 Å), 32.36° (2.764 Å), 33.08° (2.706 Å) and 43.29° (2.088 Å), and several small peaks at 21.60° (4.111 Å), 35.32° (2.539 Å), 35.59° (2.521 Å), 50.47° (1.807 Å), 51.46° (1.774 Å), and 56.39° (1.630 Å) (the value in the bracket is the lattice spacing d corresponding to the 2θ value). The lattice spacings corresponding to the peaks and those of several relevant materials consisting of Cu, In and O elements are listed in Table 4.1.

First of all, $Cu_2In_2O_5$ phase was not found, in agreement with Wada et al.'s report that $Cu_2In_2O_5$ phase could not be synthesized at below 900 °C. Secondly, metallic copper and Cu_2O phases were excluded because the peaks in the XRD patterns do not match with the data of Cu and Cu_2O JCPDS Card files. The standard XRD peaks of Cu_2O (JCPDS Card File, 05-0667) and Cu (JCPDS Card File, 85-1326) are listed in Table 4.2 for comparison. The peak at 35.59° and the hump at around 46.6° can only be assigned to monoclinic CuO (002) and ($\bar{2}02$),

Table 4.1: Peaks determined from XRD and their lattice spacings (LS), and the peaks of relevant materials $CuInO_2$, In_2O_3, and CuO with the relative lattice spacings (LS) from JCPDS Card files. The underlined are 3 strongest peaks (see Fig. 4.1)

XRD peak position (LS(Å))	Peak (LS(Å))/plane			
	$CuInO_2{}^{I}$	$In_2O_3{}^{II}$	$In_2O_3{}^{III}$	CuO^{IV}
21.60°(4.111)	...	...	21.49°(4.131) /(211)	...
<u>30.93°(2.889)</u>	31.67°(2.822) /(101)	30.97°(2.885) /(104)	30.58°(2.921) /(222)	...
<u>32.36°(2.764)</u>	32.94°(2.715) /(012)	32.59°(2.745) /(110)	...	32.49°(2.753) /(110)
<u>33.08°(2.706)</u>	...	...	33.10°(2.704) /(321)	...
35.32°(2.539)	...	...	35.46°(2.530) /(400)	...
35.59°(2.521)	...	...	...	35.50°(2.526) /(002)
43.29°(2.088)	...	...	43.80°(2.085) /(400)	...
46.62°(1.871)	...	...	...	46.56°(1.869) /($\overline{2}$02)
50.47°(1.807)	...	50.22°(1.815) /(116)	51.02°(1.788) /(440)	...
51.46°(1.774)	...	52.41°(1.744) /(122)	...	51.02°(1.788) /(112)
56.39°(1.630)	...	...	55.98°(1.641) /(611)	...

I Ref. [8]. The 2θ value was calculated from the lattice spacing;
II JCPDS Card File, 73-1809, structure-Rhombohedral, space group- R $\overline{3}_c$(167);
III JCPDS Card File, 76-0152, structure-Cubic, space group- $I2_13$(199);
IV JCPDS Card File, 80-1917, structure-Monoclinic, space group-C_c(9).

respectively. Therefore monoclinic CuO phase was confirmed.

In Table 4.1, it is noted that lattice spacings of rhombohedral In_2O_3 (104) and (116) planes are very close to those of cubic In_2O_3 (222) and (440) planes, respectively, which makes it difficult to identify the peaks at 30.93° and 50.47°. However, two reasons can exclude the existence of the rhombohedral In_2O_3 phase.

Table 4.2: Standard XRD peaks of Cu_2O (JCPDS card file, 05-0667) and Cu (JCPDS card file, 85-1326).

	2θ	*(hkl)*	d spacing		2θ	*(hkl)*	d spacing
Cu_2O	29.58	(110)	3.018 Å	Cu	43.32	(111)	2.087 Å
(PDF file:	36.44	(111)	2.464 Å	(PDF file:	50.45	(200)	1.808 Å
05-0667)	42.33	(200)	2.133 Å	85-1326)			

The first, probably the most important, is that rhombohedral In_2O_3 is a high pressure and temperature phase. As to our best knowledge, rhombohedral In_2O_3 can hardly be formed under low pressure conditions, although Sorescu et al. [97] reported nano-crystalline rhombohedral In_2O_3 synthesized by hydrothermal and postannealing pathways in a normal atmosphere at 500 °C. The second is that cubic In_2O_3 matches all the remaining peaks except the ones belonging to monoclinic CuO. $CuInO_2$ phase can also be excluded because the substrate temperature is 100 °C higher than its decomposition point, i.e. 600 °C [13]. Based on the above discussion, we can draw a conclusion that the main phases observed in the films are cubic In_2O_3 and monoclinic CuO.

The hump at around 35.9° for the film prepared on silicon substrate at 600 °C might be of cubic In_2O_3 (400) and/or monoclinic CuO (002) and (111) whose lattice spacings are very close. The small grain size also makes it difficult to differentiate these planes. The small peak at 54.20° belongs to cubic In_2O_3 (600), and this peak was not observed in other spectra (see Fig. 4.1 (a) and (b)).

The morphologies of the films characterized by AFM are shown in Fig. 4.3. The surface roughnesses (root mean square) of the films prepared at 400, 500, 600, and 700 °C were 2.93, 1.20, 1.11, and 2.31 nm, respectively, which indicated that the films became flatter as the substrate temperature increased from 400 to 600 °C. It

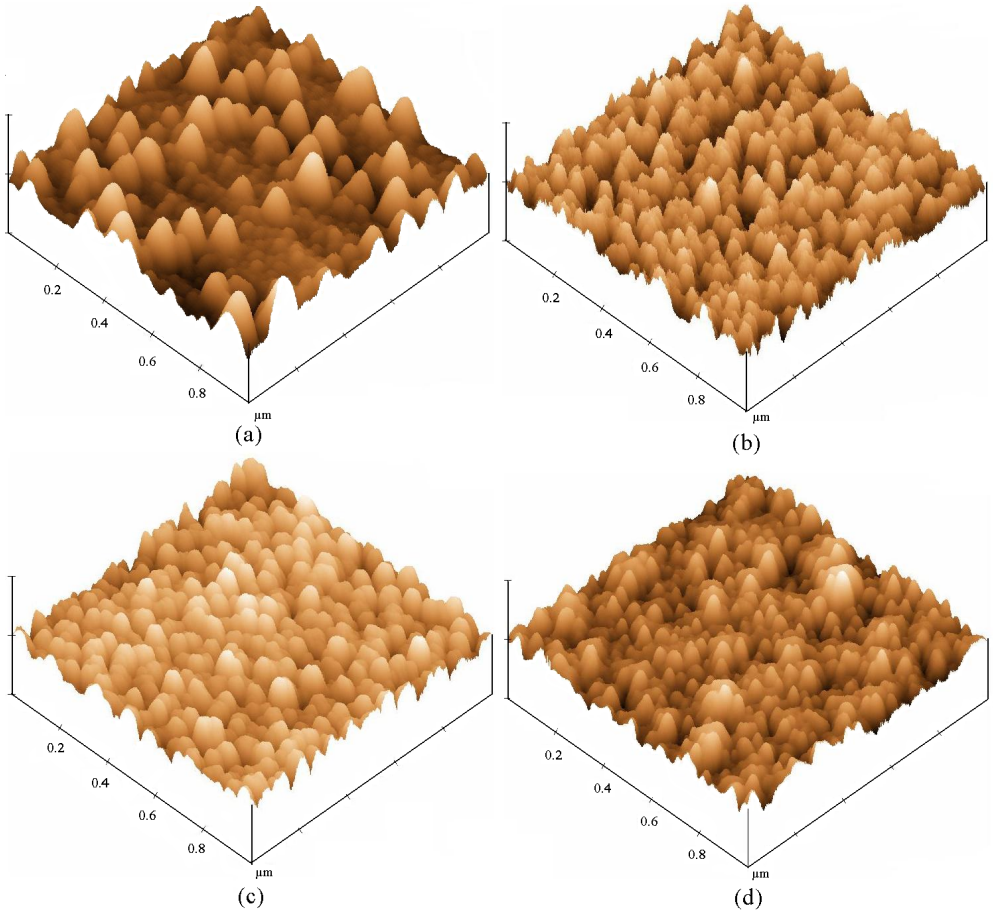

Figure 4.3: AFM images of films prepared on (100) silicon substrate at different substrate temperatures of (a): 400 °C, (b): 500 °C, (c): 600 °C, and (d): 700 °C. The corresponding scale of the z axis is 20, 20, 35, and 35 nm, respectively.

is reasonable that higher substrate temperature provided more energy for adsorbed atoms to move across the surface and led to the decrease of surface roughness. For the film deposited at 700 °C, its relatively high roughness might arise from its large crystalline grains. This abrupt increase in roughness proposes that there is no strong crystallization in the films when the substrate temperature was below 600 °C; in other words, it is hard to prepare polycrystalline Cu-In-O thin films under 600 °C using the precursors with M ratio of 1. Thus, the preparation of crystalline $CuInO_2$ thin films by PE-CVD technique is not applicable.

4.1.2 Effects of argon, oxygen flow rates and working pressure

In addition to the temperature effect, the effects of Ar and O_2 flow rates were also investigated. First, Cu-In-O films were grown on x-cut quartz substrate with the plasma power at 150 W, working pressure at 8 Pa, oxygen flow rate at 40 sccm, and substrate temperature at 600 °C. The argon flow rate and growth rate of the films are shown in Table 4.3.

Table 4.3: Gas flow rate and growth rate of Cu-In-O films prepared on x-cut quartz substrate at 600 °C.

Sample	O_2 flow rate (sccm)	Ar flow rate (sccm)	Growth rate (nm/min)
A	40	10	3.0±0.1
B	40	20	3.6±0.1
C	40	35	4.6±0.05
D	40	60	5.5±0.05

The thicknesses of samples A to D were measured to be 167±4, 182±4, 232±2, and 274±2 nm, respectively. The corresponding growth rates were 3.0±0.1, 3.6±0.1, 4.6±0.05, and 5.5±0.05 nm/min, respectively. When the argon flow rate increased, the growth rate increased in an approximately linear way (see Fig. 4.4) following the relationship of Y = 2.794 + 0.046X, where Y and X represent the growth rate and argon flow rate, respectively. When the argon flow rate increased, more precursors were transported by the carrier gas argon to the surface of substrate, resulting in a higher growth rate. Thus, mass transportation seemed play a very important role in determining the deposition rate.

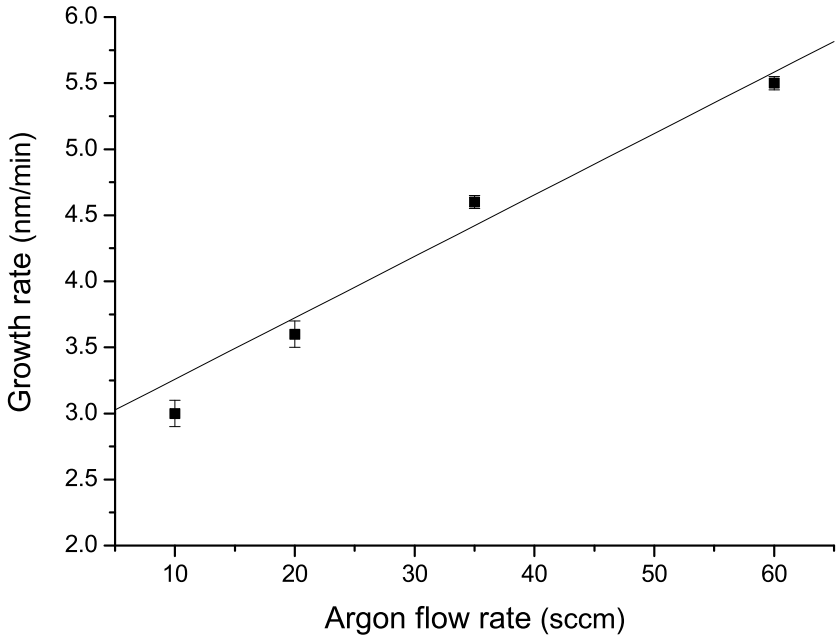

Figure 4.4: Growth rate versus argon flow rate for Cu-In-O films prepared on x-cut quartz substrates at 600 °C. A linear fitting was employed to the experimental data.

To find out the effect of oxygen flow rate, two samples E and F of the distinct oxygen flow rates of 40sccm and 5 sccm were prepared. Table 4.4 lists the growth conditions of samples E and F, whose XRD patterns are shown in Fig. 4.5.

Table 4.4: Deposition conditions for the study of the effect of O_2 flow rate and working pressure on Cu-In-O films prepared on x-cut quartz at 600 °C.

Sample	Working pressure (Pa)	O_2 flow rate (sccm)	Ar flow rate (sccm)
E	8	40	35
F	8	5	35
G	12	40	20
H	6	40	20

Referring to Table 4.1, all the peaks were indexed to cubic In_2O_3 and monoclinic CuO. As the oxygen flow rate changed from 5 sccm of sample F to 40 sccm of sample E, no significant structural difference was found from their XRD patterns. The similarity in the growth rate and film structure indicated that the

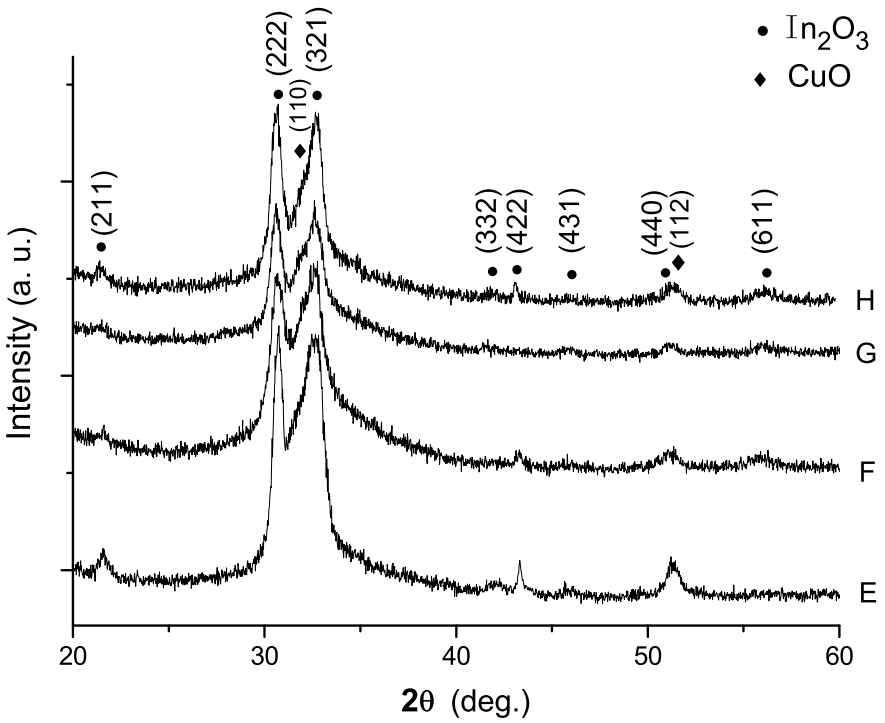

Figure 4.5: X-ray spectra of Cu-In-O films prepared under different conditions on x-cut quartz substrate at 600 °C.

effect of the oxygen flow rate was small. Thus it was not attempted to grow and characterize more samples with small variations of oxygen flow rate. The effect of working pressure was also examined. No obvious structural dependence on the working pressure was found from the XRD patterns of samples G and H prepared at significantly different working pressures of 12 Pa and 6 Pa, as shown in Fig. 4.5. The growth conditions for these two samples are given in Table 4.4 as well. Based on these results, the changes in the oxygen flow rate and working pressure seemed not to obviously affect the structure and phase composition of the films.

In Chapter 2, the fabrication of delafossite $CuInO_2$ from the parent elements has been introduced to be not energetically economical from calculating the formation energies of $CuInO_2$ and the end-point binary compounds Cu_2O and In_2O_3.

Although there has been no report of phase diagram of Cu-In-O system as to our best knowledge, the CuO phase found in the samples agrees with the equilibrium phase diagram of the Cu-O system shown in Fig. 4.6. In this phase diagram, there

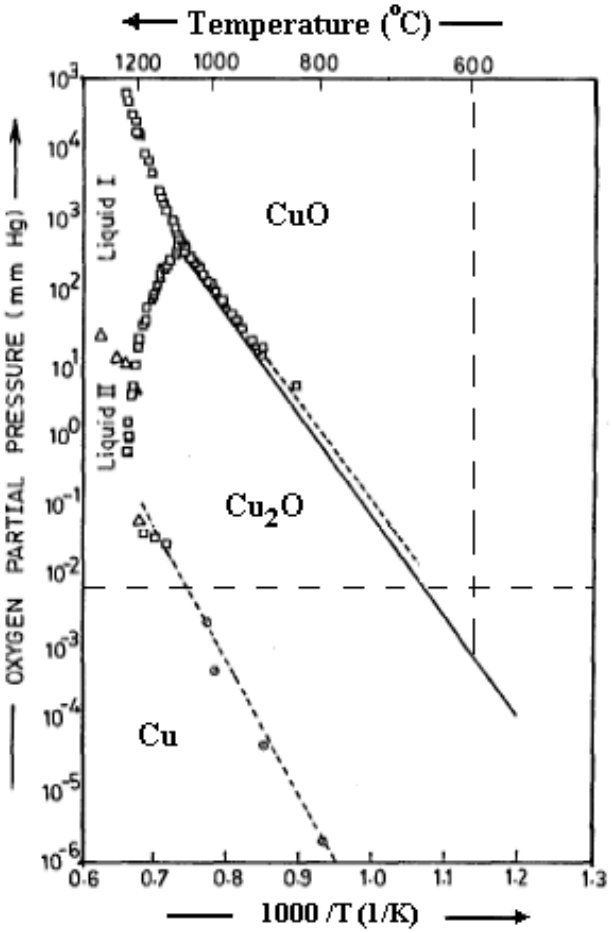

Figure 4.6: The copper-oxygen phase diagram (Adapted from Ref.[1]).

are three distinct regions corresponding to the three phases of the Cu-O system viz. CuO, Cu_2O, and pure Cu. When the temperature is below 600 °C and oxygen partial pressure is above 7.5×10^{-3} mmHg (=1 Pa), i.e. the minimum oxygen partial pressure used among all the samples, the equilibrium phase is CuO. It is further interesting to notice that no trace of $CuInO_2$ phase was found in the films prepared under the above preparation conditions, which agrees with the finding

that $CuInO_2$ cannot be synthesized directly by solid state reaction [13, 49, 51].

4.2 Optical and Electrical Properties

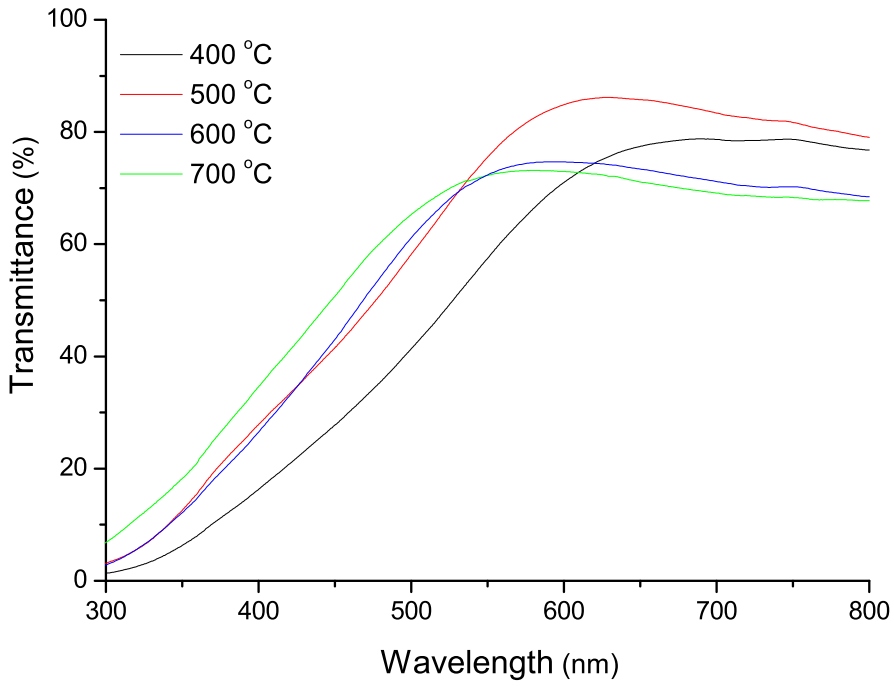

Figure 4.7: Transmittances of Cu-In-O films prepared on x-cut quartz substrate at different temperatures: 400, 500, 600, and 700 °C.

Fig. 4.7 shows transmittances of the films deposited at 400, 500, 600, and 700 °C on the x-cut quartz substrate in the wavelength range of 300-800 nm, i.e., 1.3% to 76.7%, 3.2% to 79.0%, 2.9% to 68.4%, and 6.8% to 67.7%, respectively. EDX results showed that the M ratios of the films prepared on (100) silicon substrate at 400, 500, 600, and 700 °C were 1.04±0.04, 1.34±0.02, 0.93±0.02, and 1.13±0.02, respectively.

It is well known that the d-d transitions in Cu^{2+} ions prevent a high optical transmittance in the visible range for copper(+2) oxide, however, In_2O_3 is a well-known transparent oxide, which normally has a transmission of >90% in visible range [94]. Therefore, the Cu-In-O film showed a reasonably high transmission.

The film deposited at 500 °C with the highest M ratio of 1.34 shows the highest transmittance in the range of 536 to 800 nm among the films, this film appeared slightly brown.

A shift of the absorption edge towards shorter wavelength with an increase in the substrate temperature from 400 to 700 °C was clearly observed. Following Taut's plot ($(\alpha h\nu)^{1/2}$ versus $h\nu$, where α, h and ν denote absorption coefficient, Plank constant, and photon frequency, respectively), the indirect optical band gaps of these films were estimated and listed in Table 4.5, since CuO is an indirect band gap oxide.

Table 4.5: The optical band gaps of the Cu-In-O thin films prepared on x-cut quartz substrate at different temperatures: 400, 500, 600, and 700 °C.

Substrate temperature (°C)	M ratio	Gap 1 (eV)	Gap 2 (eV)
400	1.04	1.68	1.94
500	1.34	1.89	2.12
600	0.93	1.84	2.17
700	1.13	2.13	2.26

Notably, there are two inflection points in the curves of all the films. The smaller optical gap (Gap1) values varied from 1.68 to 2.13 eV and the larger ones (Gap2) increased from 1.94 to 2.26 eV as the substrate temperature increased from 400 to 700 °C, as shown in Fig. 4.8. These band gaps are larger than that of CuO 1.0-1.5 eV [55, 62, 63, 66], and smaller than the indirect band gap of In_2O_3, i.e. 2.6-2.7 eV [94].

The M ratio of the film prepared at 400 °C, i.e. 1.04, lies between 0.93 (of 600 °C) and 1.13 (of 700 °C), however, its band gaps, both Gap1 and Gap2, are lower than the counterparts of the films prepared at 600 °C and 700 °C. On the

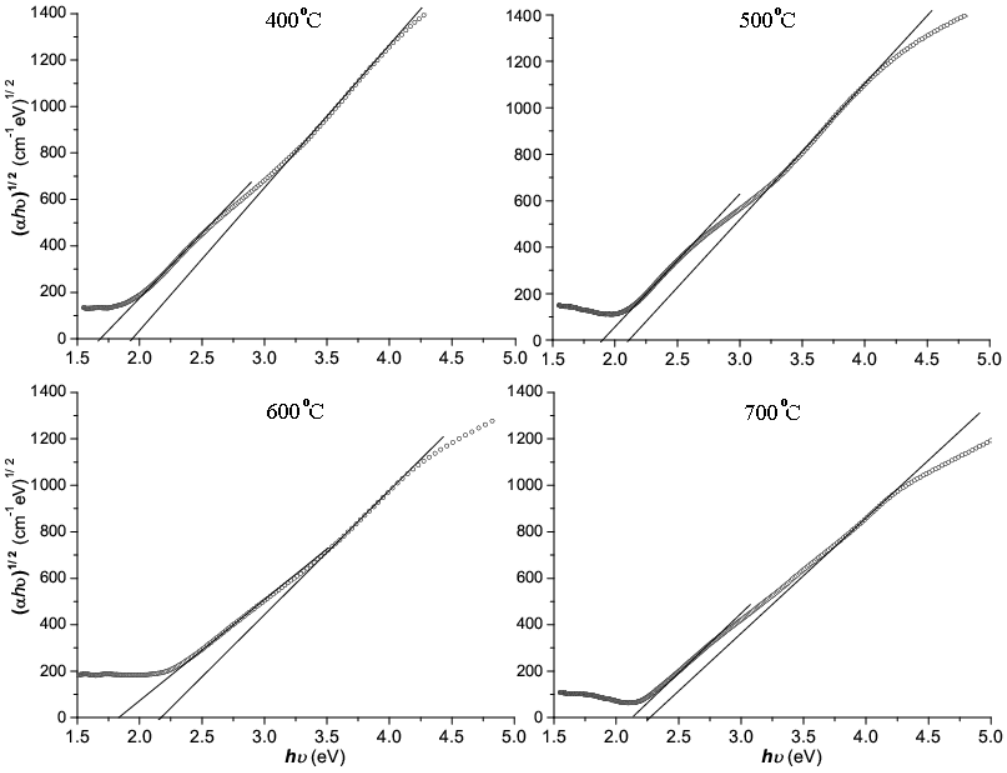

Figure 4.8: Photon energy ($h\nu$) dependence of $(\alpha h\nu)^{1/2}$, where α is absorption coefficient, h is Plank constant and ν is photon frequency, of Cu-In-O films prepared on x-cut quartz substrate at different temperatures: 400, 500, 600, and 700 °C.

other side, although the film deposited at 500 °C shows the highest M ratio of 1.34, its band gaps are 0.1-0.2 eV lower than those of 700 °C film. Therefore, it is obvious that M ratio is not a determinate factor on the band gaps of the films.

Davis-Mott model, which is used to describe the essential features of amorphous materials as shown in Fig. 4.9, was believed to be useful to explain the above phenomenon. In this band model, localized states which originate from a lack of long-rang order extend from the conduction band and valence band to form two ranges, E_A to E_C and E_V to E_B, repectively, where E_C and E_V denote the critical energies that separate the extended and the localized states. The defect states above E_B and under E_A form longer tails. The existence of localized and

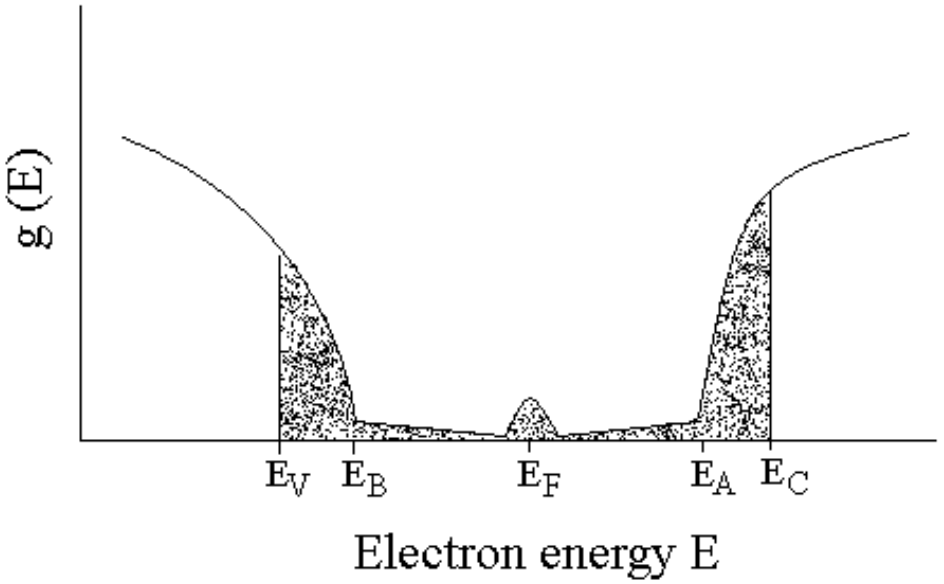

Figure 4.9: Sketch of Davis-Mott model. E_C - E_V is the mobility gap. The range E_C - E_A and E_B - E_V contain localized states originated from lack of long-rang order. E_F = Fermi energy. The distribution of localized gap states may be nonmonotonic when the defects states of a certain energy are prevalent. (Adapted from E.A. Davis and N.F. Mott, Phil. Mag. 22, 903 (1970)

defect stats should be responsible for the appearance of Gap1. When the substrate temperature increased, stronger crystallization led to a decrease in short-range order so that the position of E_A and E_B might move to E_C and E_V, respectively, resulting in an increase of optical gap as shown in Fig. 4.7. Therefore, the increase of Gap2 values with the increase of the substrate temperature was assumed to be a result of an enhanced crystallization state of the films. For the film prepared at 700 °C, its minimum difference between Gap1 and Gap2 values among all the films may suggest that localized and/or defect states have been greatly reduced by increasing the substrate temperature although the film still has amorphous part in it. The dependence of band gaps on crystallization states for some materials even in the same composition were reported in other studies. [78, 98, 99]

The Hall effect measurement was not applicable to these films due to their low conductivities. Measured by an insulating tester HEME ISO Plus, the resistances of the films were all above 2 GΩ, which means that all the films were almost insulating. Since CuO and In_2O_3 are famous p- and n-type semiconductors, respectively, a p-n junction might form at each interface between CuO and In_2O_3 phases and led to high resistance, like the cases of CuO-SnO_2 [100] and CuO-ZnO [101] heterojuntions used for gas sensors. In_2O_3 films of high resistivity (10×10^{12} Ωcm) have been reported in earlier work on the growth of In_2O_3 films by a CVD technique using $In(acac)_3$ [94]. Insulating In_2O_3 in our films could also lead to the low conductivities.

4.3 Summary

A study of copper indium oxide thin films prepared using the mixed precursors $Cu(acac)_2$ and $In(acac)_3$ with In/Cu atomic ratio of 1 under different substrate temperatures and growth atmospheres was presented for the first time. A series of experiments exploring the crystallographical behaviors of Cu-In-O system provided us an in-depth understanding of the films regarding to their structures, phase composition, electrical and optical properties.

XRD results revealed that the substrate temperature played a crucial effect on the structure of the films. The films prepared at the substrate temperature below 500 °C were amorphous in nature; when the substrate temperature increased to 600 °C and 700 °C, only CuO and In_2O_3 phases of grain size in nanometer order were found in the films. An evolution of the structures of the films from amorphous characteristic to nano-crystalline state was found as the substrate temperature increasing from 400 to 700 °C. The structure of the films did not show significant dependence on the substrate, oxygen flow rate and working pressure. The amorphous structure of the films prepared at a low temperature was explained by the overlapping of ns orbitals of transition metal (TM) cations having (n-1)d^{10}ns^0 electronic structure.

Characterized by AFM, the surface roughnesses (root mean square) of the films prepared at 400, 500, 600, and 700 °C were 2.93, 1.20, 1.11, and 2.31 nm, respectively. The abrupt increase of surface roughness of the films prepared at 700 °C was assumed to be related to its larger grain size, which implied that there is no strong crystallization when the substrate temperatures less than 600 °C.

An increase in optical band gaps with increasing the substrate temperature was found and related to the structural evolution. The appearance of double optical band gaps was observed and explained by Davis-Mott model, which suggested an existence of localized and defect states originating from short-range order. Based on the studies using different technologies, we also found that the preparation of crystalline $CuInO_2$ thin film was not applicable by using PE-CVD method in terms of crystallographical characteristic of Cu-In-O thin films.

Chapter 5

CuO:In Thin Films

In the previous chapter, Cu-In-O films prepared by using precursors $Cu(acac)_2$ and $In(acac)_3$ with unity In/Cu atomic ratio were studied. Interesting findings and a deeper understanding were achieved. However, the films obtained were insulating rather than p-type conductive, possibly due to the rich content of n-type or insulating In_2O_3 in the films. We may then need to have p-type copper oxides as the major component with the incorporation of a small amount of indium, for achieving p-type conducting films. This chapter reports on the work performed with CuO thin films incorporated/doped with indium atoms. Section 5.1-5.3 focus on the studying of the effects of the incorporation of indium on the structural, electrical and optical properties of the films, respectively. Section 5.4 presents a discussion of possible defects induced by adding indium atoms based on XPS study and their relationship with the electrical and optical properties of the films. Section 5.5 reports the effects of the substrate temperature and oxygen flow on the properties of the films prepared with precursors of the fixed M ratio of 7% in

order to verify our argument. Indium is proved to be an effective dopant to control the films' optical and electrical properties. A summary of this chapter is given in Section 5.6.

5.1 Structural Properties

Cu-In-O films were deposited on x-cut quartz (10×10 mm^2). The deposition parameters employed were: the substrate temperature at 400 °C, flow rate of reactive gas O_2 at 45 sccm, flow rate of carrier gas Ar at 25 sccm, RF discharge power at 150 W, and working pressure at 15 Pa. XRD spectra of samples A to G prepared by the mixed precursors with the M ratio of 0%, 5%, 7%, 10%, 15%, 20% and 25%, respectively, are shown in Fig. 5.1(a): the original data and (b): after smoothing by Fourier filtering, respectively. The peaks observed in the spectra arise from monoclinic CuO.

The full width half maxima (FWHM) of CuO (111) peak of samples A, B, and C was measured to be 1.00°±0.02°, 1.30°±0.05°, and 1.30°±0.05°, respectively; the corresponding grain sizes calculated by the Scherrer formula (Eq. 3.2) were estimated to be 8.4±0.2, 6.5±0.3, and 6.5±0.3 nm, respectively. A TEM picture of sample C is shown in Fig. 5.2, which verifies the existence of nano-grains and further shows that the grains are scattered in an amorphous matrix. For sample D (with the M ratio of 10%), the intensity of (111) peak decreased significantly compared to those of samples A to C, and its FWHM was measured to be about 1.5°, with a corresponding grain size of about 5.0±0.2 nm. When the M ratio reached 15% (sample E), a hump formed at the position of CuO (110) and (002) peak was observed, and the (111) peak almost disappeared. As to samples F and G, with the M ratios of 20% and 25%, respectively, the small humps forming at the three peak positions almost merged into a big hump, indicating that these films were amorphous in nature.

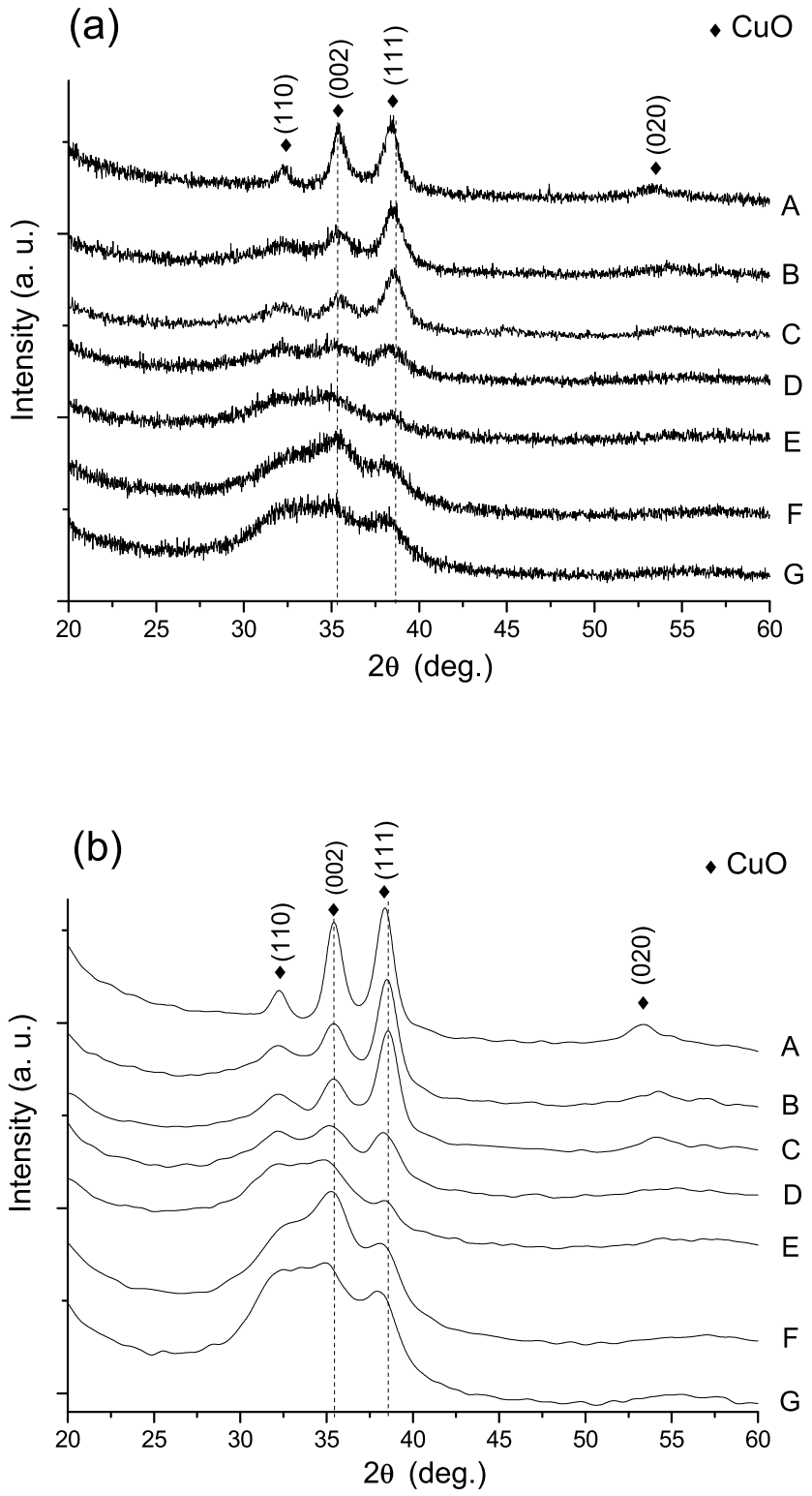

Figure 5.1: XRD spectra (a) original data and b) after Fourier filtering, of samples A to G prepared on x-cut quartz substrate at In/Cu atomic ratio of A: 0%, B: 5%, C: 7%, D: 10%, E: 15%, F: 20%, G: 25% in the mixed precursors.

Recalling the XRD spectra shown in Fig 4.1 (a) and (b), we can find that a single hump finally formed as the M ratio reached 50% for the films prepared at 400 °C on both quartz and silicon substrates. These results together present a clear picture of the evolution of the films' structures from nano-crystalline characteristic to amorphous state as the M ratios increased from 0% to 25%. Its great influence on the properties of the films will be shown in the following parts.

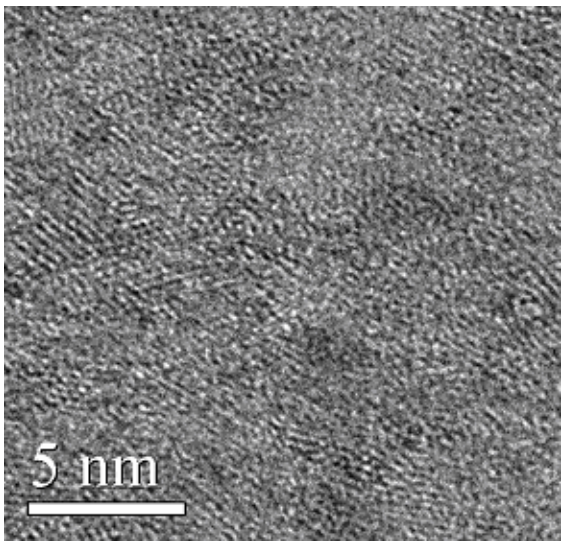

Figure 5.2: Transmission electron microscopic (TEM) image of sample C.

It was observed that there was a shift, about 0.25°, in the (111) Bragg peak towards higher 2θ as the M ratios increased from 0% to 7% for samples A to C. However, the (002) peaks do not see such a shift, which means that the spacing of *00l* planes is almost unchanged. As the M ratios increased from 7% to 25%, the (111) peaks of sample D, F and G shifted towards lower 2θ, in an opposite direction compared to the former. Thus, sample C has the lowest lattice spacing of (111) plane. Although the reason behind the shift is not clear, it is certain that size effect cannot explain it alone because the grain size of sample C is not the

minimum one. A trade off between the size effect and indium substitution was assumed to balance the shift. A further discussion will be introduced in Section 5.5.2.

EDX results showed that sample A was unintentionally doped with indium (the M ratio <1%) due to some contamination from the chamber, while the M ratios in samples B to G were 6±2%, 8±1%, 10±1%, 15±2%, 18±1%, and 25±1%, respectively, which were close to the corresponding ratios in the mixed precursors. The area for EDX signal collection was $1\mu m \times \mu m$. Since EDX is a semi-quantitative method to estimate the chemical composition, hereafter, for convenience we will still use the M ratio in the mixed precursors to denote each sample. The thicknesses of samples A to G were measured to be 85, 82, 83, 80, 85, 105, and 121 nm, respectively. The thickness deviations were less than ±5 nm for all the samples.

The surface morphologies of the films characterized by AFM are shown in Fig. 5.3. The surface roughnesses (Root mean square) of samples A to G were 2.9, 2.4, 2.3, 1.7, 1.6, 1.8, and 1.6 nm, respectively. It is clear that the roughness values for samples A to C are higher than those of samples D to G. The amorphous structure of the later samples should be the root cause of the decrease of surface roughness.

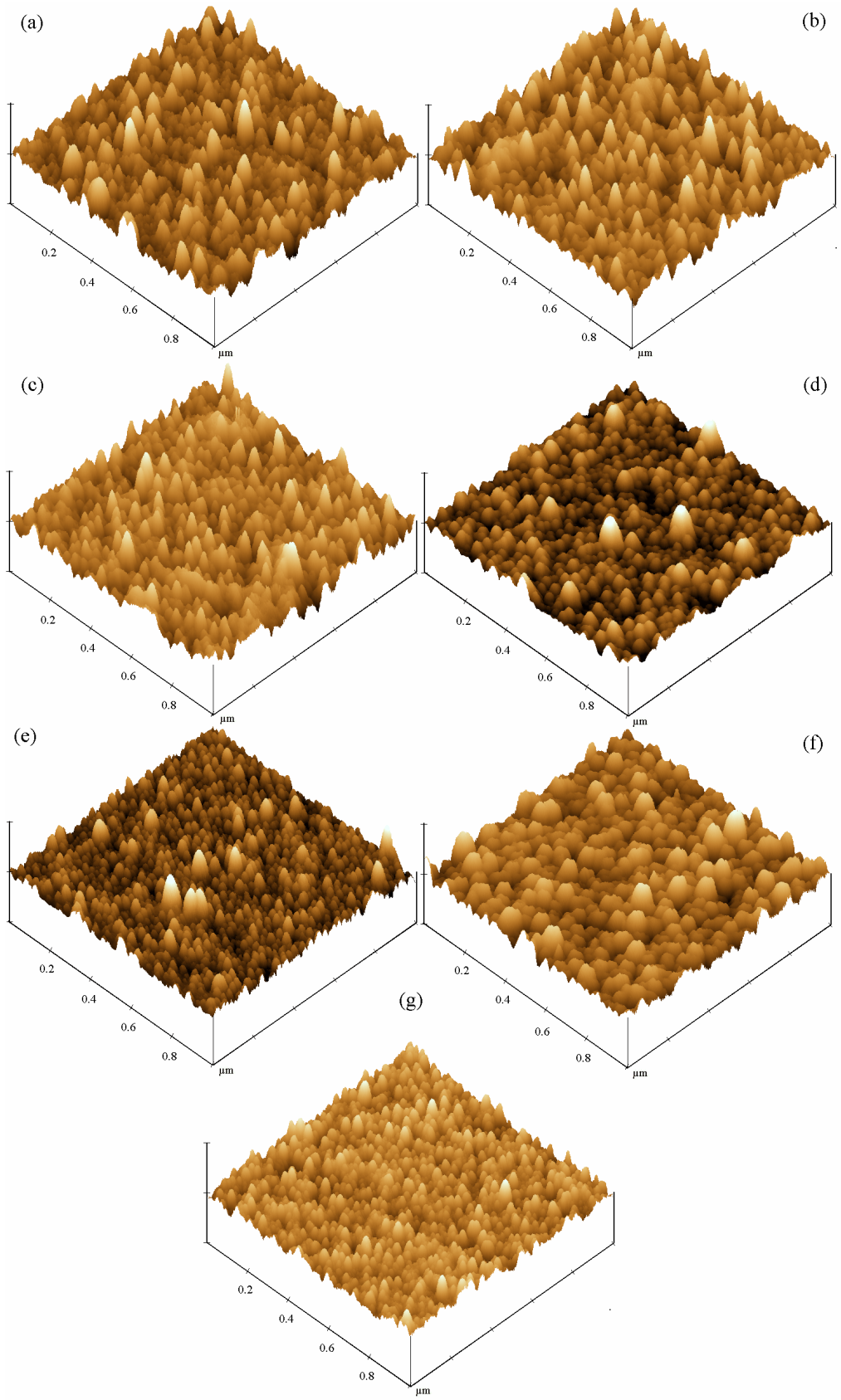

Figure 5.3: AFM images of (a) to (g) for samples A to G, respectively. The z scale is 20 nm.

5.2 Electrical Properties

The resistances of samples A, F and G were $> 2\ G\Omega$ so their resistivities were too high to be measured. The resistivities of samples B and C were 13.92 Ωcm and 7.35 Ωcm with the M ratios of 6% and 8%, respectively. As the M ratio reached 10% (sample D) and 15% (sample E), the resistivity increased to 8.73 Ωcm and 14.43 Ωcm, respectively. In summary, the resistivities first decreased from "out of range" to 7.35 Ωcm and then increased to be "out of range" again as the M ratios increased from nearly 0% to 25%. The minimum resistivity, i.e. 7.35 Ωcm, occurred at the M ratio of 8%, as shown in Fig. 5.4 .

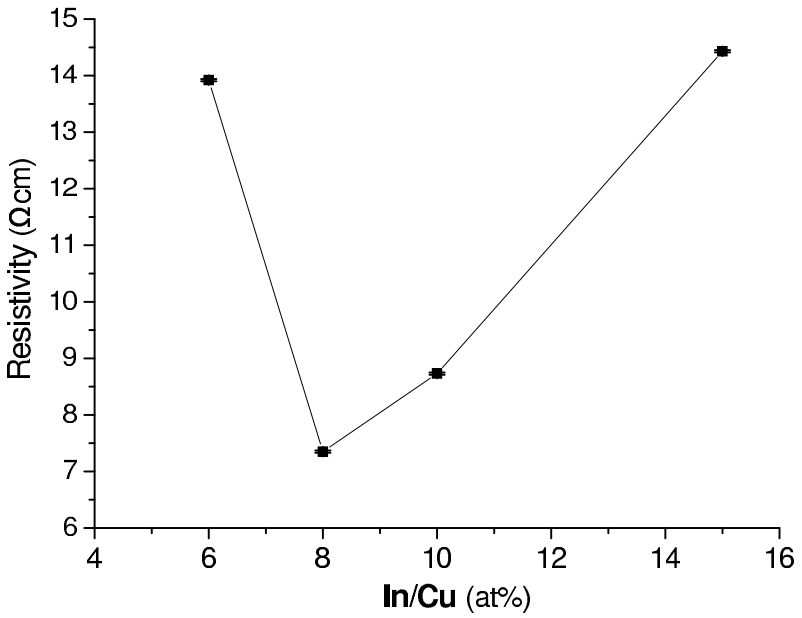

Figure 5.4: Resistivity dependence on the In/Cu mole ratio of sample B: 6%, C: 8%, D: 10%, and E: 15%.

Boucher [86] pointed out that many properties of CuO thin films are associated with the small grain size or amorphous structure. In the present case, these two factors may work together. With the increase in indium concentration, the grain

size, which is known to be critical to properties of semiconductor thin films due to quantum confinement and enhanced surface effects, decreased clearly as shown in Fig. 5.1. Meanwhile, defects induced by adding indium atoms possibly played a more important role in controlling the electrical properties of the samples than the size effect did. It is noted that the resistivity of sample C is 52.8% of sample B's, although their grain sizes are very close. Therefore the difference on the M ratio (6% vs 8%) must be a key point.

As far as possible defects are concerned, the incorporation of indium into CuO may cause two reactions, as follow:

$$\frac{1}{2}In_2O_3 + CuO \rightarrow In_{Cu}^{\cdot} + Cu_{Cu}^{'} + 2O_O^{*} + \frac{1}{4}O_2(g), \tag{5.2}$$

and

$$\frac{1}{2}In_2O_3 + \frac{1}{4}O_2 \rightarrow In_{Cu}^{\cdot} + V_{Cu}^{"} + 2O_O^{*} + h^{\cdot}, \tag{5.3}$$

where O_O^{*}, $V_{Cu}^{"}$, $In_{Cu}^{\cdot}$, $Cu_{Cu}^{'}$, and $h^{\cdot}$ denote lattice O, Cu vacancy, In substitution, lattice Cu, and hole, respectively, and the superscripts denote effective charge states: $*$ - neutral, $'$ - negative, and $\cdot$ - positive.

In view of charge balance, the neutral nature of Equation 5.1 seems to exclude it from the root cause of the low resistivities of samples B to G, however, the positive hole induced by negatively charged defect complex $In_{Cu}^{\cdot}$ and $V_{Cu}^{"}$ shown in Equation 5.2 can provide a reasonable explanation for it. It is noted that Wu and his coworkers [64] have reported that Cu vacancies are the most stable defects in Cu-rich and O-rich environments through a first-principle study by using the

LSDA+U method. That's why we argue that Equation 5.2 is valid. Chemical absorbed oxygen [18] and Cu(+1) suggested by Equation 5.1 will be discussed futher in Section 5.4.

To find out more on the electrical conduction mechanisms of these samples, activation energies of the positive holes were determined by the temperature dependence of resistance from room temperature (RT) to 80 °C in air. The activation energy Ea, conductivity σ and temperature T are related by

$$\sigma = \sigma_0 Exp(\frac{-E_a}{kT}) \tag{5.4}$$

where σ_0 is a constant, and k is Boltzmann's constant. A linear relationship between ln(1/R) and 1/T was observed for the conductive samples B to E, indicating typical semiconductor characteristic (see Fig. 5.5). The activation energies for samples B to E were 0.154 eV, 0.140 eV, 0.165 eV, and 0.208 eV, respectively. The error was less than 0.005 eV for all the samples. These values are lower than the activation energy of the sputtered CuO films at about 300K (0.22 eV) [81]. Jeong and Choi [102] reported that conduction of $Cu_{1-y}O$ was due to the hopping of the charge carrier with activation energy of 0.1 eV and suggested that the activation was not due to charge carrier generation but to electrical mobility. The trend of the activation energy is consistent with that of the resistivity for samples B to E, which suggests that the smaller activation energy for the positive holes might be a reason for the lower resistivities of the samples.

"Sign abnormal", the sign change of the Hall coefficient, which prevents proper estimation of the Hall mobility and the number of free carriers, was observed for

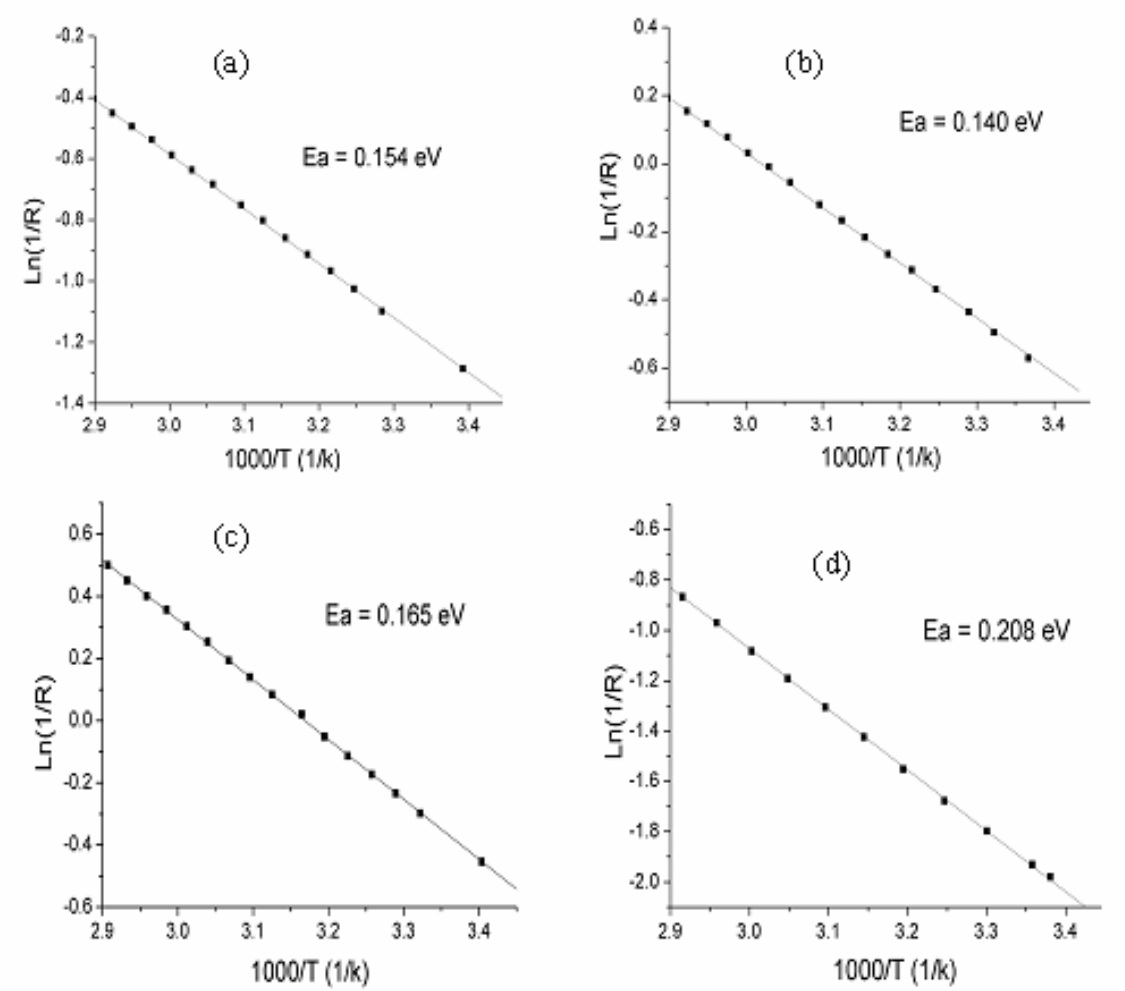

Figure 5.5: Natural logarithm of inverse of resistance as a function of temperature for samples B to E. Figure (a), (b), (c), and (d) belong to samples B to E, respectively. The unit of resistance R is MΩ.

samples B to E. For example, the Hall coefficient of sample C varied from -7.32 to +5.93 m^2/c and corresponding carrier concentration from -8.5×10^{18} to +1.8×10^{20}, although its resistivity remained almost constant. The anomalous sign in the Hall coefficient can occur near the mobility edge if the mean free path of carriers is shorter than a critical value [103]. In small microcrystallites, all states are discrete and localized since the number of atoms is small. Therefore, the scattering occurs primarily in the localized states, like tail states, and the effective mass of a free

charge changes its sign as it crosses the mobility edge [104]. In our case, the "Sign abnormal" literally reflects the existence of localized states as explained by the Davis-Mott model in Chapter 4. Seebeck voltages at the cold end of our conducting samples B, C, D and E were positive, indicating p-type conductivity.

The co-doping theory [44] may be useful in understanding these smaller activation energies. Yoshida and co-workers employed this theory to interpret the p-type conduction of a few wide-band-gap semiconductors such as GaN, ZnSe, and ZnO. Their calculation revealed that the simultaneous co-doping of n-type and p-type dopants led to a decrease in the Medelung energy. Therefore, p-type dopant incorporation was enhanced. According to this principle, $In_{Cu}^{\cdot}$ and $V_{Cu}^{"}$ may work as n-type and p-type dopants respectively, in our case, and the difference is that $V_{Cu}^{"}$ is not an exterior dopant but a vacancy. The low activation energies of the films seem to suggest that the positive holes induced by the defect complex ($In_{Cu}^{\cdot}$+ $V_{Cu}^{"}$) might be weakly localize to the copper vacancies.

5.3 Optical Properties

Fig. 5.6 shows transmittances of samples A to G in the range of 300-800 nm. The transmittances of the samples were all below 56% at 800 nm and below 21% at 400 nm, indicating that these films are semi-transparent in the visible range.

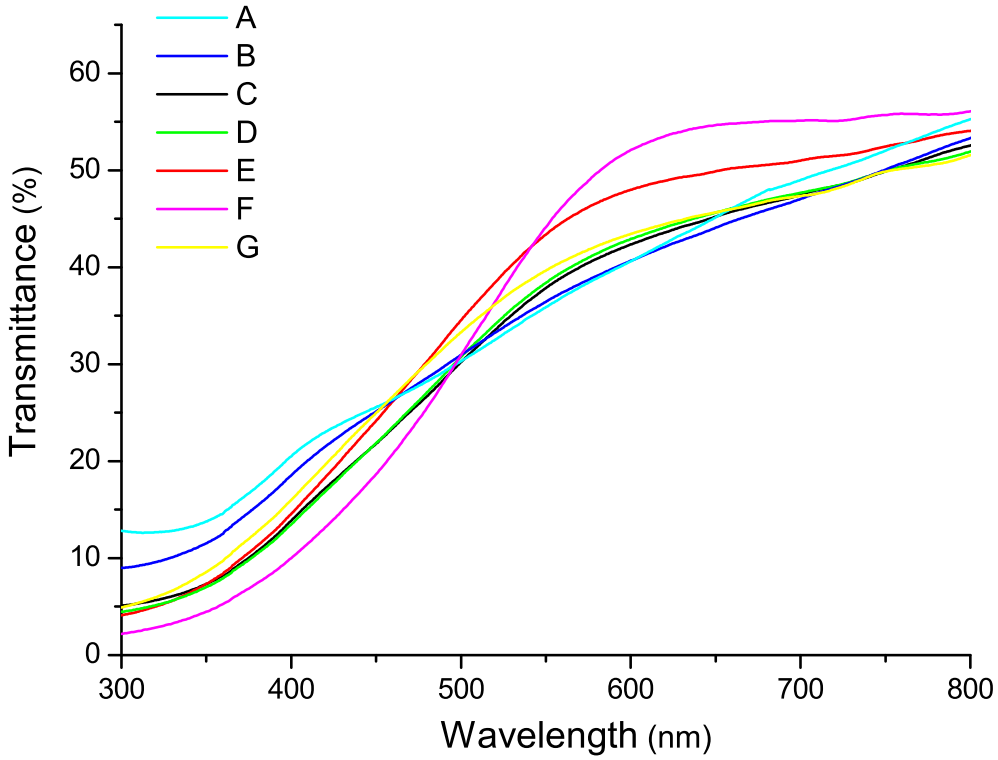

Figure 5.6: Transmittances of samples A to G.

The optical band gaps of the films were deduced from the absorption measurement by the Tauc plot of $((\alpha h\nu)^{1/2}$ versus $h\nu)$, where α, h and ν denote absorption coefficient, Plank constant, and photon frequency, respectively, as shown in Fig. 5.7. Similar to Fig. 4.8, two inflection points in the curves were observed for the samples. The corresponding Gap1 and Gap2 values are listed in Table 5.1. Gap2 was estimated to be 1.42, 1.47, 1.56, 1.67, 1.72, 1.64, and 1.75 eV for samples

A to G, respectively, which are larger than the reported band gaps of CuO (1.0-1.5 eV) [55, 62–64], and much lower than the indirect band gap of In_2O_3 (2.6-2.7 eV) [94]. To estimate the possible experimental error for these band gap values, a sample thickness variation (±10 nm) for each sample was assumed in calculating α, and all the resulted gap deviations were less than 0.03 eV.

Table 5.1: The optical band gaps of samples A to G.

Sample	M ratio	Gap 1 (eV)	Gap 2 (eV)	Gap2-Gap1 (eV)
A	<1%	0.91	1.42	0.51
B	6%	0.95	1.47	0.52
C	8%	0.87	1.56	0.68
D	10%	0.97	1.67	0.70
E	15%	0.98	1.72	0.74
F	18%	0.75	1.64	0.89
G	25%	0.86	1.75	0.89

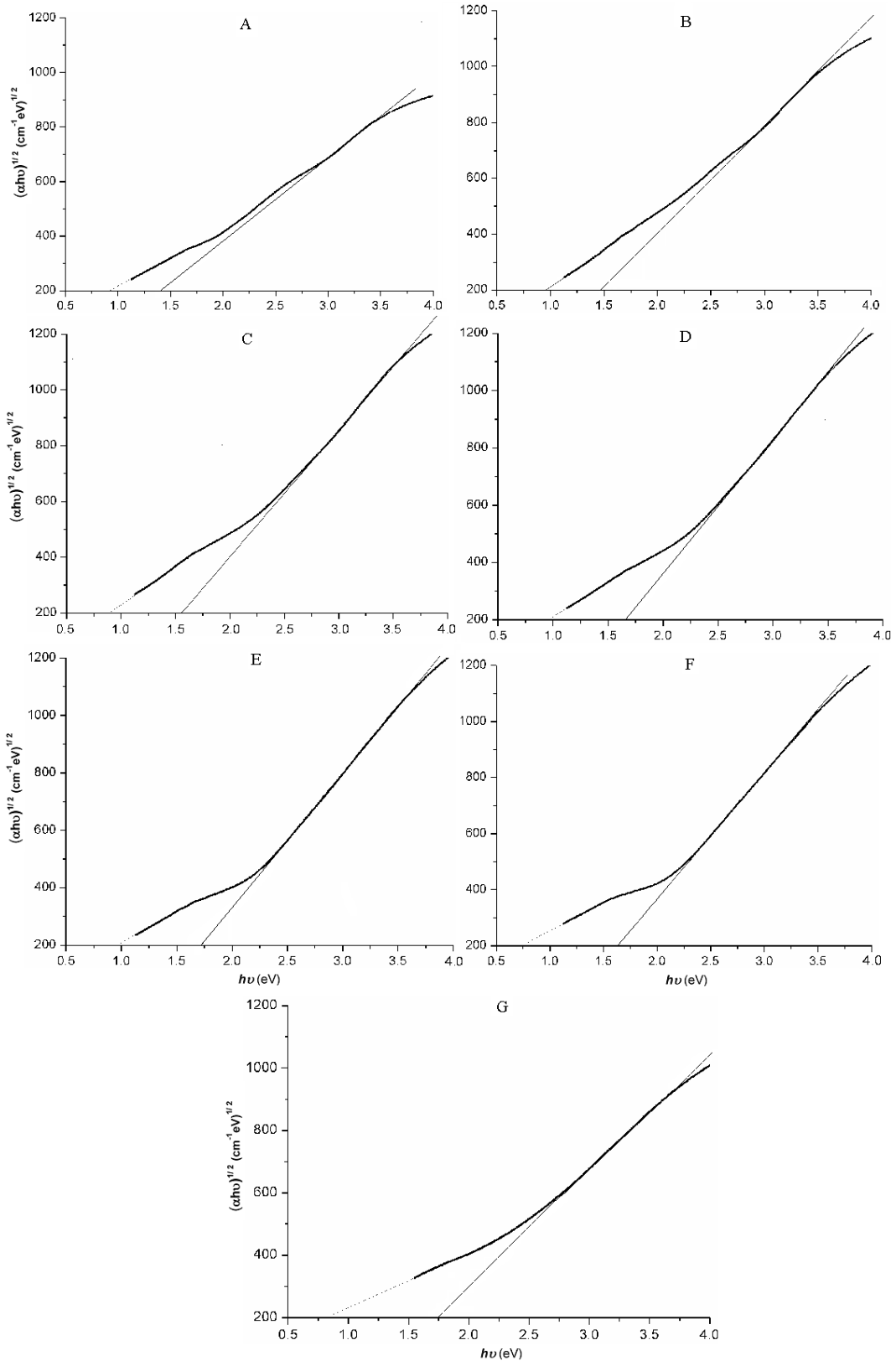

Figure 5.7: Photon energy ($h\nu$) dependence of $(\alpha h\nu)^{1/2}$ for samples A to G, where α is absorption coefficient, h is Plank constant and ν is photon frequency.

It is well known that in the $3d$-transition metal (TM) oxides, the oxygen $2s$ and $2p$ orbitals overlap strongly with the cation $4s$ and $4p$ orbitals, which leads to a strong hybridization. A large energy gap exists between the top of the $2p$ and the bottom of the $4s$ and $4p$ bands. All the $3d$-sub-bands lie within this energy band gap [105]. Based on the molecular description [106–108], the so-called cluster model describes the electronic structure of $3d$-TM compounds in terms of three parameters: the charge transfer (CT) energy Δ required to transfer an electron from a ligand valence orbital (in our case O $2p$) to the TM $3d$ shell; the Coulomb interaction Udd between two $3d$ electrons; and the hybridization V between the ligand and TM valence orbitals. Although the Coulomb interaction Udd plays a major role in the electronic structure of CuO [109], Zimmermann et al. [109] pointed out that an increase in covalency between TM $3d$ and ligand valence states (e.g. O $2p$) promotes a delocalization of TM $3d$ electrons, which means more hybridization between the ligand and TM valence orbitals can increase the $3d$-band width. Therefore, the increased differences between Gap1 and Gap2 of the samples A to G (see Table 5.7) might benefit from an wider $3d$-sub-bands caused by the $3d$ orbital hybridization associated with indium ions in the form of Cu-O-In bonding. Furthermore, with adding more indium into the samples, the chemical composition of samples D to G was gradually away from CuO and more and more In-O bonding would form in the samples, resulting in the increase of the Gap2 values.

As to the Gap1, Narushima and his coworkers [110] have reported a similar phenomenon in their studying of amorphous ZnO-Rh_2O_3 thin films, in which two optical band gaps were found and the smaller one was considered to be due to tail

absorption instead of the band gap of ZnO or Rh_2O_3. We believe that the Gap1 in our case are also from the tail absorption considering the amorphous parts in our samples. The reasons that the Gap1 and Gap2 were not assumed to be the band gap of CuO and In_2O_3, respectively, are as follows,

First of all, for samples A to C there was only crystalline CuO phase revealed by XRD (see Fig. 5.1) as the In/Cu atomic ratios were less than 0.07. It seems not be reasonable to accept that the appearance of the Gap2 of sample A is due to indium doping of <1%; in other words, the band gap of In_2O_3 could hardly be applied to explain the Gap2 at least for samples A to C.

Secondly, the Gap2 values (1.42-1.75 eV), as mentioned earlier, were far away from the band gap of In_2O_3, i.e. 2.6-2.7 eV, although the Gap1 values (0.75-0.95 eV) were rather close to the reported CuO band gap, i.e. 1.0-1.5 eV. Someone argues that the Gap2 line should intersect with the extended Gap1 line drawn in dash instead of the X-axis, however, such method has never been reported for the Tauc plot as to our best knowledge.

Finally, the Tauc plot has been widely used to estimate the optical band gap of materials in singe phase, however, it is difficult to make a conclusion whether it is still applicable to measure the individual optical band gap of multiple phases in a sample, considering some complicate factors such as interface, microstructure, and composition, etc. The Tauc plots of our films with nano-particles and amorphous matrix seemed manifest that the tail absorption due to the amorphous parts played a more important role in determining the optical properties of the films than the indirect band gaps of CuO and/or ino nano-particles.

The variations of the resistivity, activation energy and optical band gap with the In/Cu mole ratio in the samples of A to E are shown in Fig. 5.8.

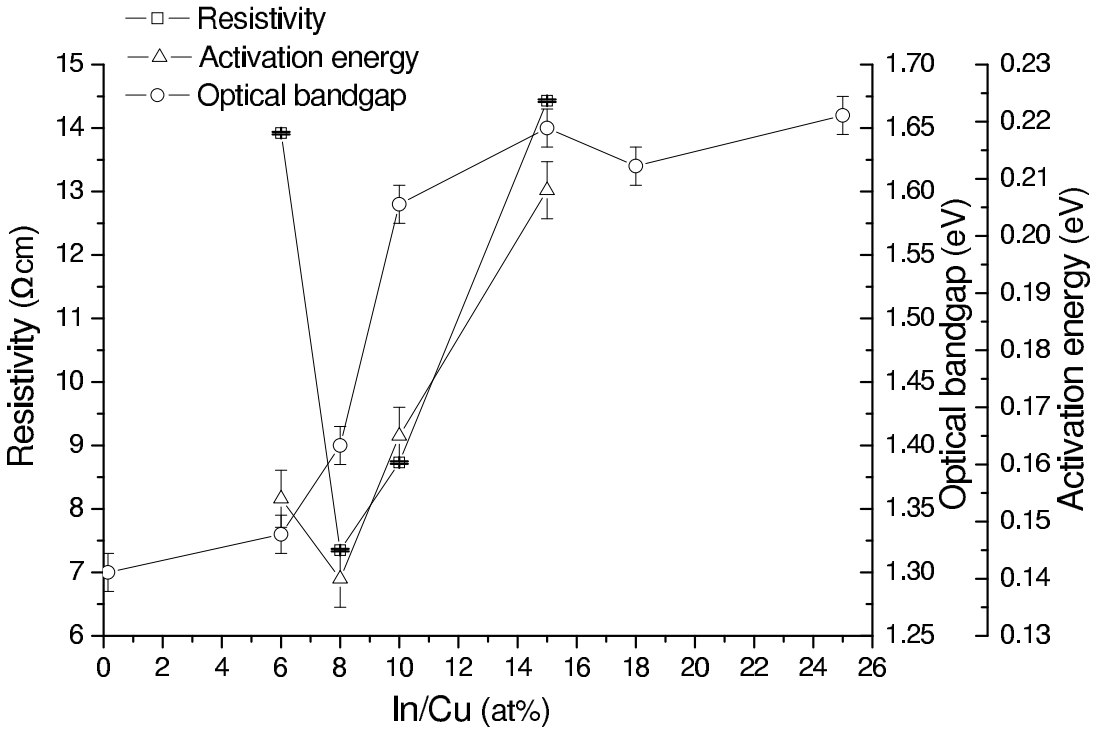

Figure 5.8: Resistivity, optical bandgap, and activation energy variation with respect to the In/Cu mole ratio of sample A: <1%, B: 6%, C: 8%, D: 10%, E: 15%, F: 18%, and G: 25%.

It is obvious that these three curves have similar trends when the M ratio of the films exceeds 8%. As the M ratio increased over 20%, samples G and F were almost insulating, which might be due to n-type or insulating amorphous In_2O_3 in the films as explained in Chapter 4. It is reasonable that more In-O-In bonding would form as more indium atoms were added in the films, no matter in amorphous matrix or crystalline CuO grains. Therefore, it suggests that low resistivity and high optical band gap cannot be achieved simultaneously by increasing indium concentration alone.

5.4 X-ray Photoelectron Spectroscopy Study

XPS spectra of Cu $2p^{3/2}$ core level of samples A, B, C, E, and G are shown in Fig. 5.9 (a) to (e), respectively. All the curves were calibrated by taking the C1s peak as 284.8 eV. The samples were first sputtered for 1 minute with an Ar ion beam of 2 keV to remove contamination from the surface. All the curves were peak fitted by the software Multipal V 8.0 using a Shirley type base line with Gauss-Lorentz profiles, and five binding energy states denoted by five peaks were revealed in each spectrum. The positions and relative intensities of the peaks are listed in Table 5-1. V ratio (defined as the ratio of the sum of the areas of peaks 2, 3 and 4 (A2-4) to that of peak 1 (A1)) was calculated for each sample and also listed in Table 5.2.

Table 5.2: XPS peak fitting results for samples A, B, C, E and G. The two numbers for each peak stand for the relative area (%) (the value on the top) and binding energy (eV) (the value in the bottom parentheses), respectively. V denotes the ratio of the sum of the areas of peaks 2, 3 and 4 to that of peak 1.

	A	B	C	E	G
Peak 1	60.03 (932.7)	73.39 (932.5)	62.95 (932.7)	86.25 (932.6)	87.70 (932.6)
Peak 2	22.85 (933.8)	15.11 (933.7)	21.82 (933.9)	5.10 (933.7)	5.20 (933.7)
Peak 3	6.25 (941.3)	3.48 (940.9)	7.37 (941.3)	1.45 (941.1)	1.03 (941.1)
Peak 4	8.83 (943.9)	5.32 (943.9)	5.65 (943.9)	3.91 (943.9)	3.24 (943.8)
Peak 5	2.04 (946.8)	2.71 (946.5)	2.21 (946.7)	3.29 (946.6)	2.83 (946.5)
V	0.63	0.33	0.55	0.12	0.11

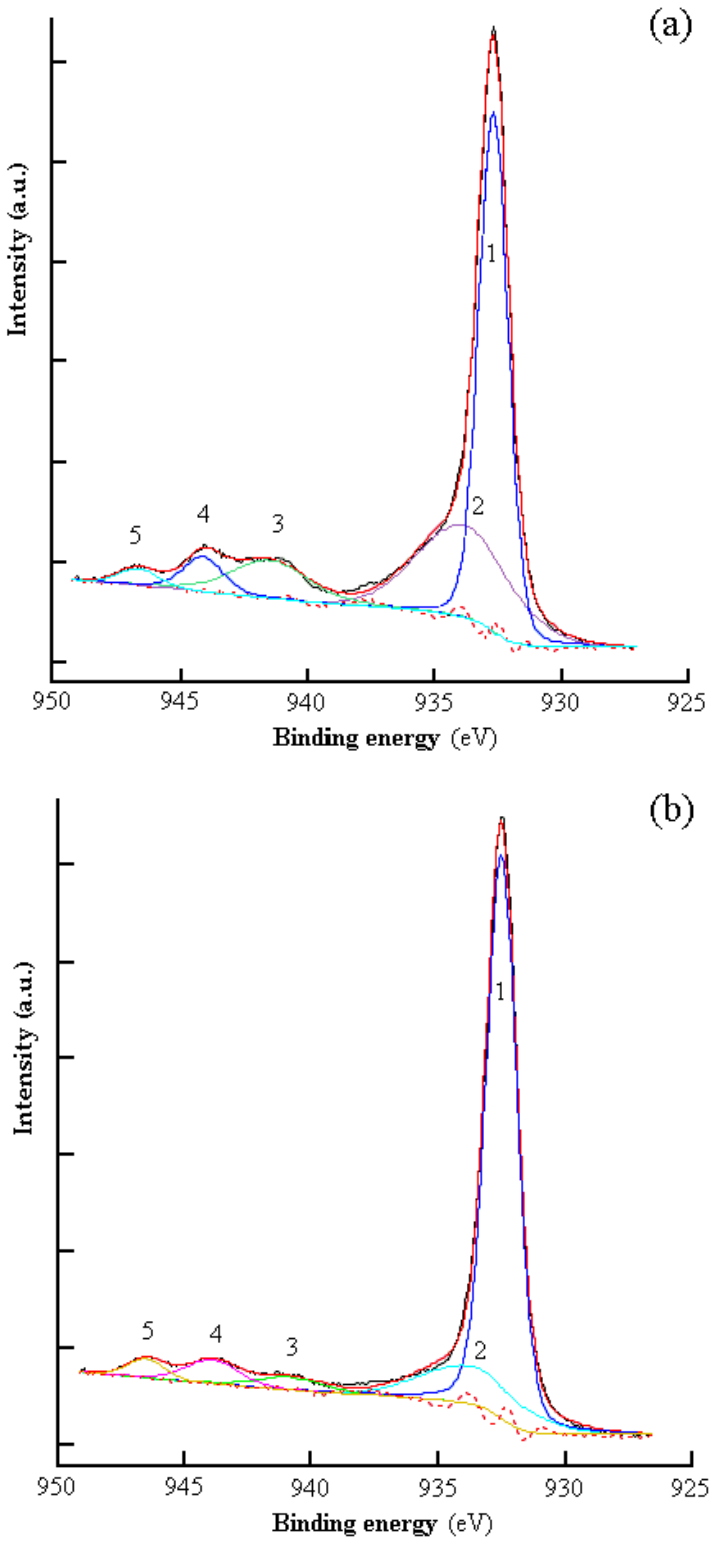
(a)
Intensity (a.u.)
1
2
3
4
5
950
945
940
935
930
925
Binding energy (eV)
(b)
Intensity (a.u.)
1
2
3
4
5
950
945
940
935
930
925
Binding energy (eV)

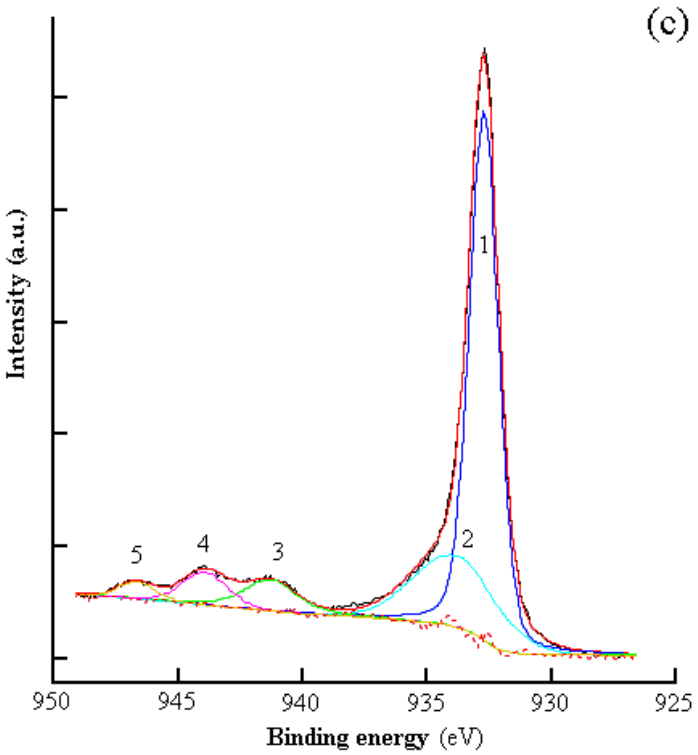
(c)
Intensity (a.u.)
1
2
3
4
5
950
945
940
935
930
925
Binding energy (eV)

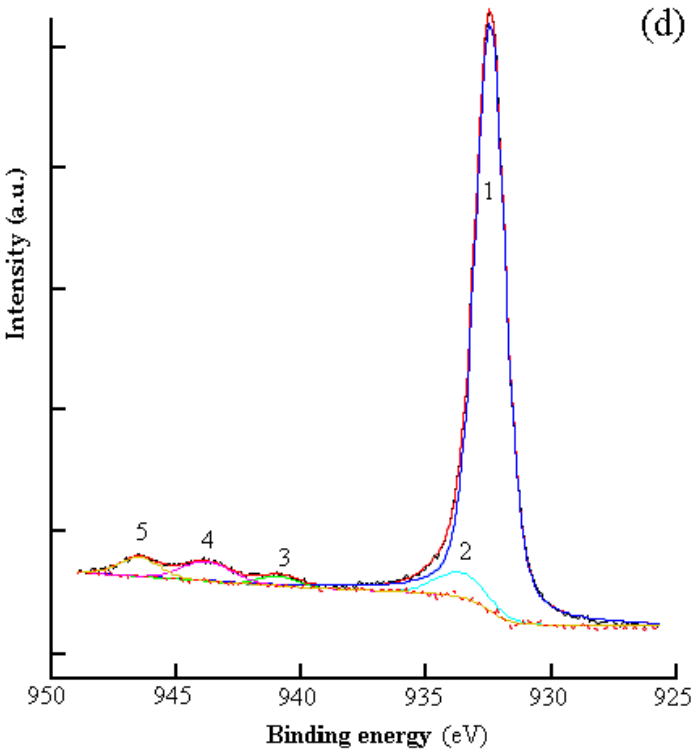
(d)
Intensity (a.u.)
1
2
3
4
5
950
945
940
935
930
925
Binding energy (eV)

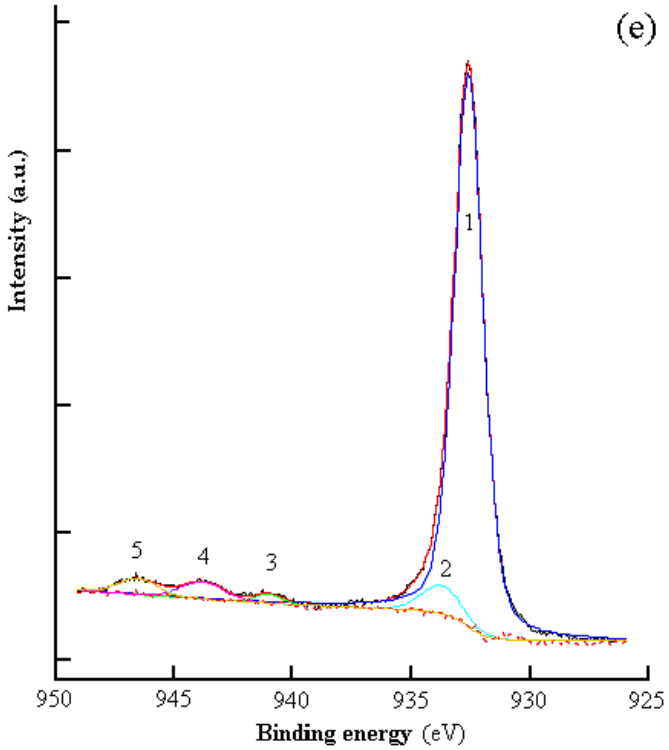

Figure 5.9: XPS spectra of Cu $2p^{3/2}$ core level with peak fitting obtained by using a Shirley-type base line with Gauss-Lorentz profiles. Spectra (a), (b), (c), (d) and (e) belong to samples A, B, C, E, and G, respectively. The outside red line is the experimentally obtained curve.

As shown in Fig. 5.6, all the spectra show two binding energy states at around 932.5-932.7 eV (peak 1) and 933.7-933.9 eV (peak 2), which correspond to Cu(+1) and Cu(+2), respectively. The reduction of Cu(+2) to Cu(+1) during XPS analysis has been widely reported in the literature and has been attributed to the integrated X-ray dose, heating from X-ray gun, outgassing in a vacuum, and slow electrons emanating from the X-ray window during analysis [111]. Cox [105] pointed that the creation of a core hole in X-ray photoemission experiments produces a strong perturbation which can redistribute valence electrons. Thus the strongest peaks (peak 1 in our case) appearing in the XPS of copper oxides correspond to final states with the $3d^{10}$ configuration, whatever the oxidation state of copper. This

comes about because of the strong Coulomb interaction of the core hole with the copper $3d$ electrons. That is why our XRD results only show CuO phase in the samples, as introduced in Section 5.2, however, Cu(+1) dominates in the excited states probed by photoemission. Nevertheless, some useful information can still be extracted from the relative intensity of the excited and initial states, i.e. Cu(+1) and Cu(+2), respectively. The V ratio, which can measure the relative amount of Cu(+2) to Cu(+1) [111], was found to be 0.63, 0.33, 0.55, 0.12, and 0.11 for samples A, B, C, E, and G, respectively (the introduction of peak 3 and 4 will be presented later). Since the highest V ratio, i.e. 0.63, appeared in sample A, whose M ratio is lower than 1%, it indicates that adding indium atoms could decrease the relative amount of Cu(+2) to Cu(+1) to different degrees for samples B to G. This phenomenon can be explained by two reasons at least. First, Chusuei et al. [111] observed that the relative amount of the Cu(+2) to Cu(+1) reduction induced by X-ray would increase as the copper oxide particle size decreased. The decreased grain sizes observed in samples B to E as introduced above would contribute to the lower V ratios according to Chusuei et al.'s principle. Secondly, because the electronegativity of indium atom (1.78)* is lower than that of copper (1.90)*, indium loses its electrons more easily to O than Cu. We can expect that the electronegativity of the oxygen in Cu-O-In bonding with respect to Cu is lower than that in the Cu-O-Cu bonding, which leads to an increase of covalent component of Cu-O bonding. Thus, the incorporation of indium atoms helped to increase the d^{10} character of the main peak and caused a higher Cu(+1)/Cu(+2) ratio, which is exactly what Equation 5.1 expresses.

Nevertheless, considering the almost same grain sizes of samples B and C intro-

duced in Section 5.2.1., the highest V ratio of sample C suggests that the grain size did not dominate the V ratios alone. The interaction between the core holes left by emitted electrons and the holes induced by the indium inclusion as introduced in Equation 5.2 might redistribute the valence electrons, which was assumed to be responsible for the high V ratio of sample C.

Finally, the origin of the holes induced by the indium inclusion should not come from Cu(+1), an acceptor state for CuO. Ohya et al. [16] suggested the addition of Al_2O_3 into CuO lattice might cause a reduction of Cu(+2) into Cu(+1) as described by the following equation,

$$\frac{1}{2}Al_2O_3 + CuO \rightarrow Al_{Cu}^{\cdot} + Cu_{Cu}^{'} + 2O_O^{*} + \frac{1}{4}O_2. \tag{5.5}$$

which is same in principle with Equation 5.1. However, a combination of the lowest resistivity and a high V ratio (0.55) observed in sample C can exclude the possibility that most of the holes in this sample came from Cu(+1), otherwise sample C should have the lowest V ratio among all the samples. Because all the samples have been sputtered with an Ar ion beam of 2 keV for one minute before the collection of XPS spectra (10 nm SiO_2 can be removed as a reference), the chemisorbed oxygen as suggested by Suda et al. [18], if there is any, would be removed by the sputtering and therefore contribute nothing to the variation of the V ratios.

Peaks 3-4 denote the well-known shake-up satellites of Cu $2p^{3/2}$ core level, and the presence of such shake-up satellites is diagnostic, in a "fingerprint" mode, of an open $3d^9$ shell of Cu(+2) [112]. The shake-up satellites may appear when

the outgoing photoelectron simultaneously interacts with a valence electron and shakes it up to any empty level during the relaxation process; the energy of the core electron is then reduced slightly, giving a satellite structure a few electron volts below (but above on a binding-energy scale) the core level position. Regarding to CuO, O $2p$-to-Cu $3d$ charge transfer transition is generally accepted as the source of the satellite peaks [113, 114] and the structure in the satellite line is due to the multiplet splitting of the $2p^5 3d^9$ final state (with core hole present, the $2p^5 3d^{10}$ initial state is pulled down by the core hole-$3d$ interaction to the $2p^5 3d^9$ final state to screen effectively the core hole formed during the final-state relaxation) [55].

The separation energies between the satellites (peak 3) and main peak (peak 1) were 8.6, 8.4, 8.6, 8.5, and 8.5 eV for sample A, C, E, and G, respectively. These values are larger than the 7.7 eV reported by Scrocco [115]. Yin et al. [116] reported that the separation between the satellite and the parent line increased as the ligand becomes less electronegative, e.g., the separation ΔE follows the order with the ligands I > Br > Cl > F. The increase of covalent component of Cu-O bonding due to indium doping as mentioned above may explain the increased separation energies according to Yin et al.'s principle.

According to our knowledge, the new satellite feature at 946.7±0.2 eV (peak 5) has never been reported, for CuO or Cu_2O. This feature may be related to the presence of In, since all the samples contain In atoms. The areas of peak 5 were 2.04, 2.71, 2.21, 3.29, and 2.83 for samples A, B, C, E, and G, respectively, indicating a small fluctuation. However, the areas of peaks 3-4 are proportional to the area of peak 2 as shown in Table 5.1. From this point, multiplet splitting [55]

should not be the common mechanism for peaks 3-5. Defect energy levels induced by indium doping might be related to this new feature. Further research is needed to explicate its origin.

XPS spectra of In $3d$ and O $1s$ region of sample C are shown in Fig. 5.10 (a) and (b), respectively; the former reveals a doublet whose binding energies 444.2±0.2 eV and 451.8±0.2 eV correspond to In $3d^{5/2}$ and In $3d^{3/2}$ peaks, respectively; the later shows a characteristic peak at 530.0±0.2 eV. For all the samples, the difference in the binding energies of In $3d^{5/2}$ and In $3d^{3/2}$ peaks are almost constant and equal to 7.5 eV, in agreement with that of In_2O_3 [91].

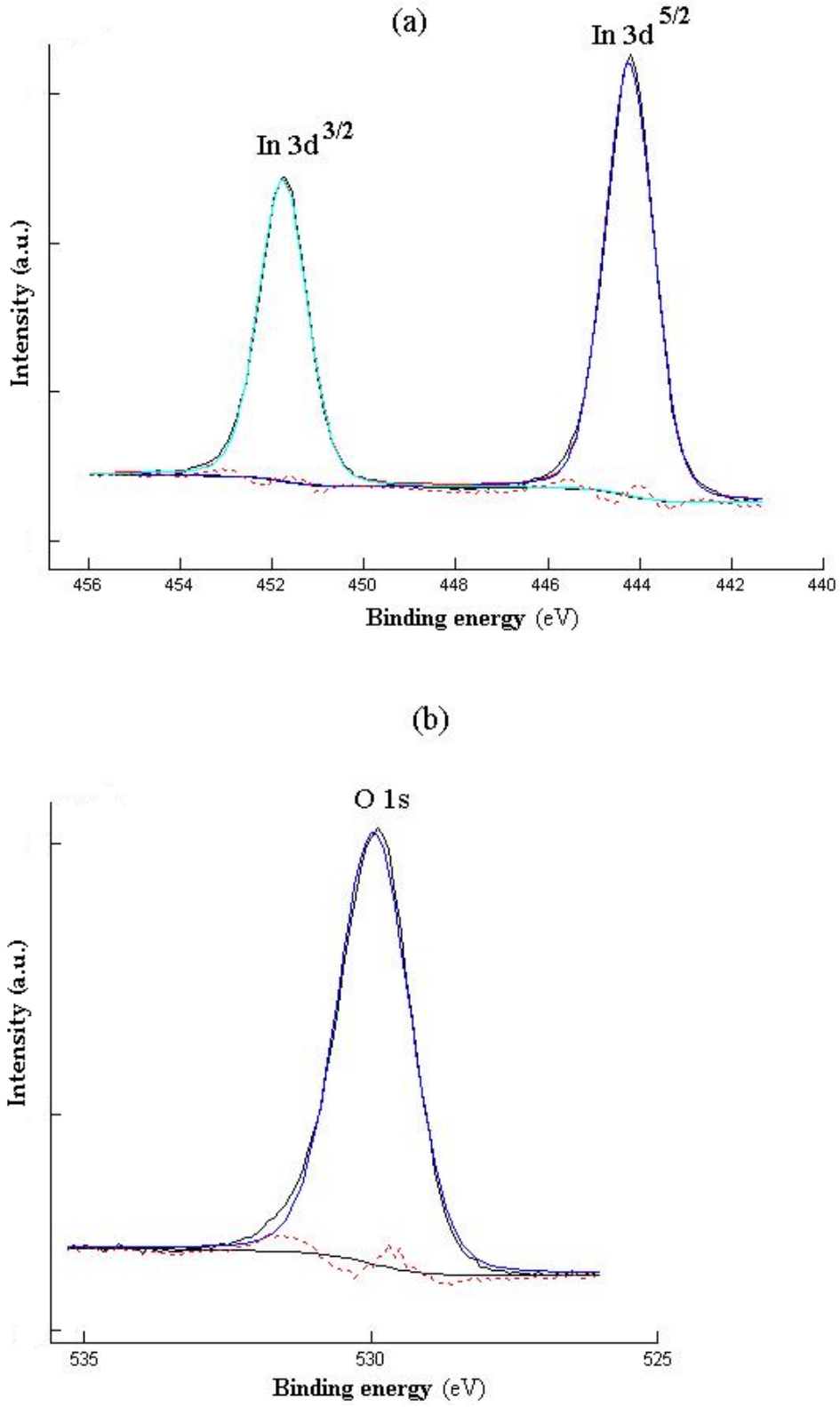

Figure 5.10: XPS spectra of (a) the In 3d region and (b) the O 1s region with curvefitting for sample C.

5.5 Effects of Oxygen Flow Rate and Substrate Temperature

5.5.1 Effect of oxygen flow rate

In this section, the effects of the oxygen flow rate and substrate temperature on the properties of the films were studied in a series of experiments, using the mixed precursors with the fixed M ratio of 7%.

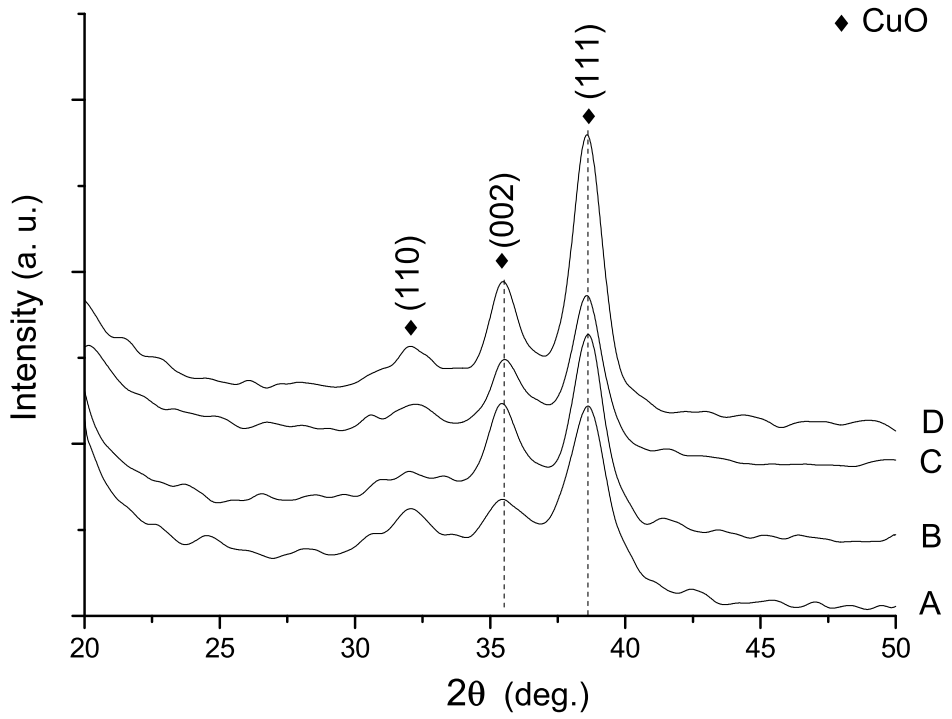

Figure 5.11: XRD spectra (after Fourier filtering) of samples prepared at the oxygen flow ratio of A: 15 sccm, B: 30 sccm, C: 45 sccm and D: 60 sccm.

Fig. 5.11 shows the XRD spectra (after Fourier filtering) of samples prepared at oxygen flow rate of A: 15 sccm, B: 30 sccm, C: 45 sccm and D: 60 sccm, respectively (at the substrate temperature: 400 °C, Ar flow rate: 25 sccm, plasma

power: 150 W, and working pressure: 15 Pa). CuO is still the only phase found in the samples, and their grain sizes are comparable, which means that the structure of these samples shows no dependence on the oxygen flow rate in the range of 15-60 sccm. The shift of CuO (111) peak observed in Fig. 5.1 did not occur in these samples, suggesting no dependence of oxygen pressure on the lattice spacing.

As shown in Fig. 5.12, when the oxygen flow rate increased from 50 sccm to 200 sccm, the resistivity decreased from 77.22±2.34, 57.72±3.05, 18.83±0.02 to 15.11±0.64 Ωcm, respectively. EXD analysis showed that the M mole ratio in the samples were 9±2%, 6±1%, 7±1%, 6±1%, which were close to those in the precursors.

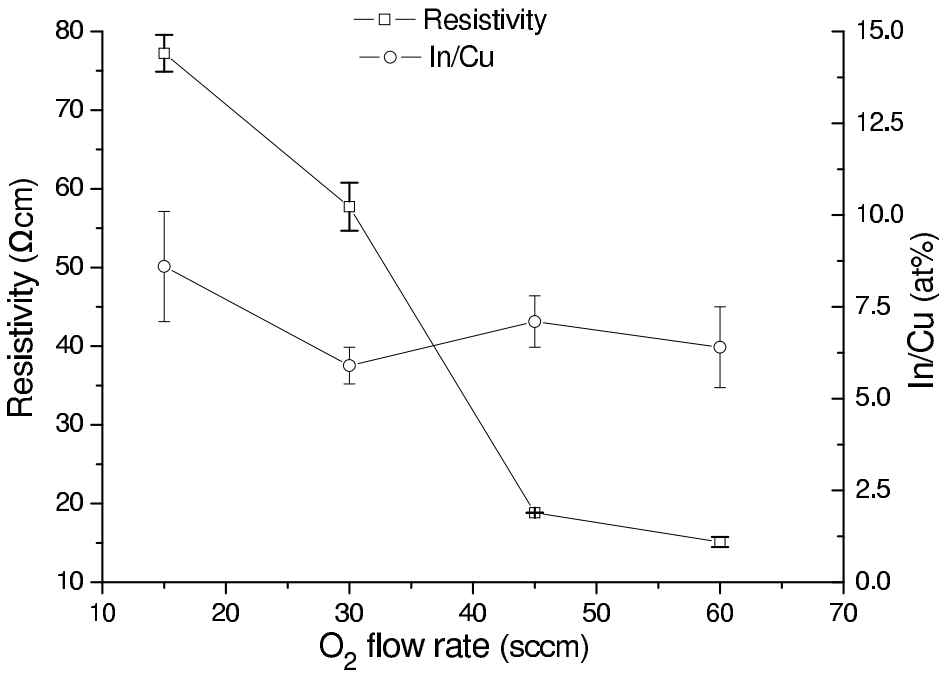

Figure 5.12: Resistivity versus oxygen flow rate and In/Cu mole ratio in films deposited at substrate temperature of 400 °C.

The decrease of the resistivity with the increase of the oxygen flow rate can be easily explained by Equation 5.2. As oxygen pressure increased, the reaction would

move to the right side, resulting in more holes and therefore lowering resistivity. Meanwhile, it was observed that when the oxygen flow rate was over 45 sccm, the rate of resistivity decreasing reduced, which suggested that the hole concentration might be close to saturation, as the oxygen pressure was high enough to oxidize most of the incorporated indium atoms to form defect complex ($In_{Cu}^{\cdot}$+ $V_{Cu}^{''}$). At the same time, recalling the lowest resistivity mentioned in Section 5.2, namely 7.35 Ωcm at the M ratio of 8% and the same O_2 flow rate of 45 sccm, the resistivity of these thin films might have a stronger dependence on indium concentration than on oxygen partial pressure, especially when the oxygen flow rate was over 45 sccm.

5.5.2 Effect of substrate temperature

The substrate temperature strongly influenced both the film structure and the resistivity. Fig. 5.13 shows the XRD spectra of samples E, C, F, and G prepared at 300, 400, 500, and 600 °C, respectively (at the O_2 flow rate: 45 sccm, Ar flow rate: 25 sccm, plasma power: 150 W, and working pressure: 15 Pa).

Increasing the substrate temperature clearly changed the film structures in the XRD spectra where sample E deposited at 300 °C gived an amorphous pattern and sample G at 600 °C depicted a different texture orientation, with different relative intensity of the peaks compared to samples C and F at 400 °C and 500 °C. It is obvious that a hump around 41.3° appeared for samples F and G. In_2O_3 (420) and (332) plans are the only two planes close to the hump position among possible phases, namely CuO, Cu_2O and In_2O_3. Furthermore, there was a shift, about 0.34°, in the CuO (111) Bragg peak towards lower 2θ with the substrate

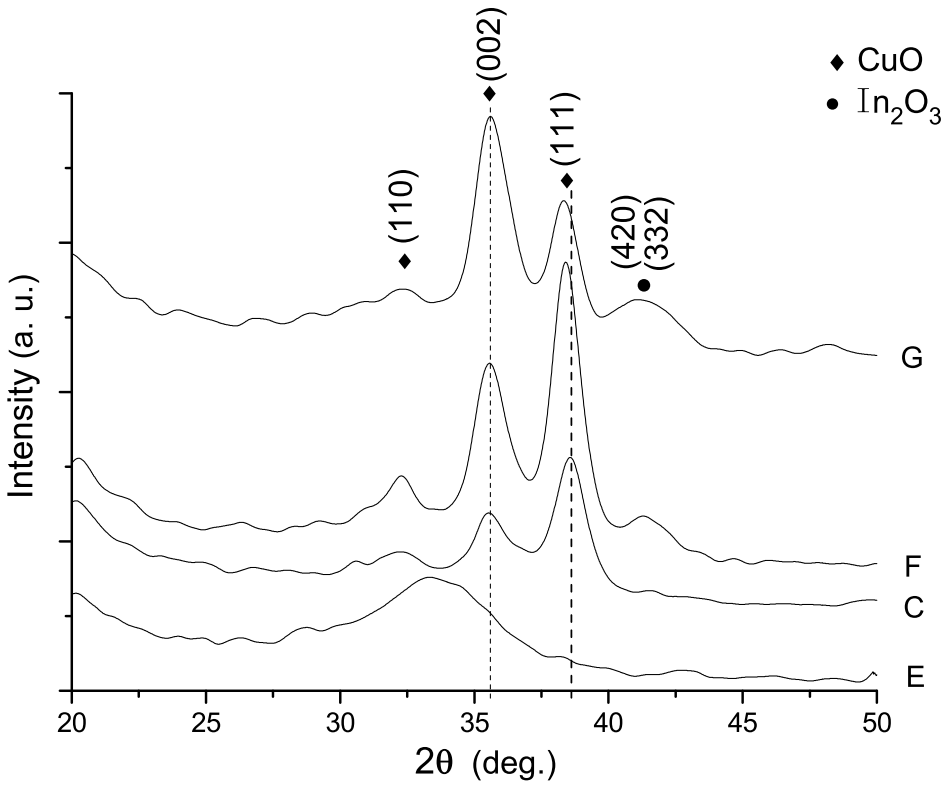

Figure 5.13: XRD spectra (after Fourier filtering) of samples E, C, F, and G deposited at 300 °C, 400 °C, 500 °C, and 600 °C, respectively.

temperature increasing from 400 to 600 °C, however, no such shift was found for the CuO (002) peaks. The FWHM of CuO (111) peaks of samples C, F, and G were measured to be 1.30°±0.05°, 1.15°±0.05°, and 1.20°±0.05°, respectively; the corresponding grain sizes calculated by the Scherrer formula (Eq. 3.2) were estimated to be 6.5±0.3, 7.3±0.3, and 7.0±0.3 nm, respectively. If the 2θ shift of the CuO (111) Bragg peak was mainly due to the size effect, the sample F, with the largest grain size among these three samples, should shift the most taking sample C as a reference. However, the maximum shift occurred on sample G. These results proved that there was no correlation between the grain size and lattice spacing of (111) planes, which excluded the size effect from the root cause of the shift. At the same time, the appearance of In_2O_3 phase in samples F and G reminded us that

the concentration of indium atoms in CuO lattice might play a important role on the degree of the shift as well as lattice spacing. The similar shift mentioned in Section 5.1 (see Fig.5.1) could support this argument, in which the degree of the shift seemed to be correlated with the In/Cu concentration in the samples whose M ratios were <1%, 6±2%, and 8±1%. A more detailed structure study is needed to further verify this conclusion.

The thicknesses of samples E, C, F and G were 50±3, 86±4, 93±4, and 98±4 nm, respectively; corresponding to growth rates of 0.5±0.05, 1.5±0.05, 1.9±0.1, and 2.1±0.1 nm/min, respectively. As the substrate temperature increased from 300 to 400 °C, the deposition rate increased by almost 3 times. However, from 400 to 600 °C the increase of deposition rate was only about 40%. The strong dependence of chemical reaction on substrate temperature limited in some degree the application of PE-CVD in fabricating CuO thin films at lower temperatures.

The resistivity of sample E was 8.82±0.35 Ωcm, and for F and G their resistivities were too high to be measured. The M ratios of samples E, F and G detected by EDX lie between 6% to 7%. The deviation is less than 1%. The increase of resistivity with the increasing substrate temperature suggests that the Cu vacancy formation enthalpy is negative, which has been reported in previous CuO studies [102, 117]. In our case, by increasing the substrate temperature the precursor $In(acac)_3$ seems to have been oxidized to form In_2O_3 phase instead of forming the defect $In_{Cu}^{\cdot}$. Holzschuh and Suhr [76] has reported that elevated substrate temperature led to under-stoichiometric in oxygen for films prepared by PE-CVD with $Cu(acac)_2$. The low resistivity of the film deposited at 300 °C, i.e. 8.82 Ωcm,

possibly came from its amorphous structure due to the lower substrate temperature. This result proves again that the small grain size is not the root cause of the low resistivity, which has been mentioned in Section 5.2, and the stoichiometry in the disordered part of the films probably played a more important role on the resistivity.

Fig. 5.14 shows transmittances of samples E, C, F, and G in the wavelength range of 300-1000 nm. A shift of absorption edge towards shorter wavelength with the increase of the substrate temperature from 500 to 600 °C can be clearly observed. However, the film prepared at 300 °C (sample E) did not show an abrupt drop at the whole range and its transmittance smoothly dropped from 64.5% at 1000 nm to 4.6% at 300 nm, which is obviously different from those of samples F and G. It reflects that the localized states caused by the amorphous structure

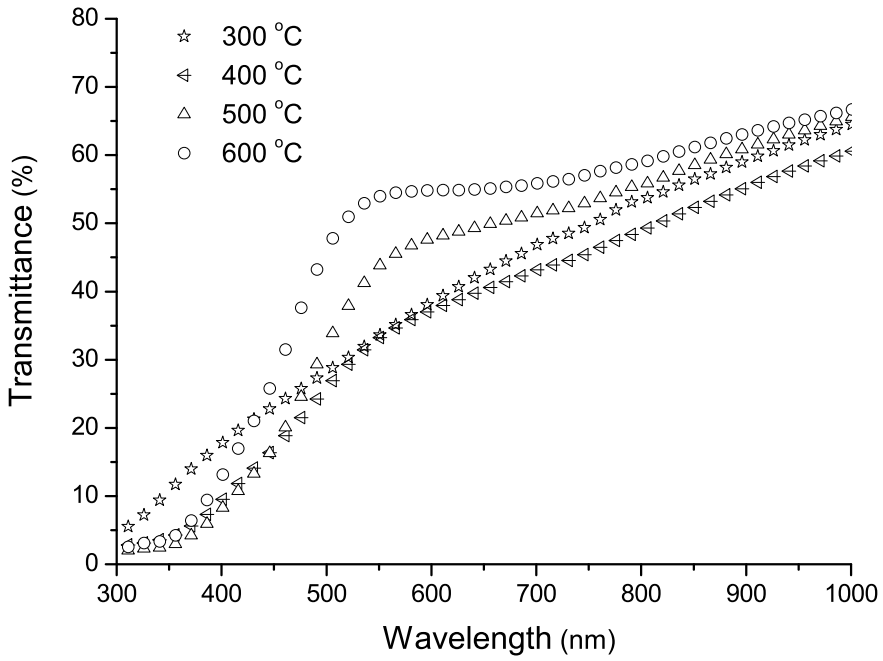

Figure 5.14: Transmittances of CuO thin films deposited at different substrate temperatures: 300, 400, 500, and 600 °C.

form continue energy levels, instead of a band gap. Taut's plots ($(\alpha h\nu)^{1/2}$ versus $h\nu$) were used to estimate the optical band gap of these films. The band gaps of samples E, C, F, and G were estimated to be 1.25, 1.37, 1.55, and 1.71 eV, respectively, as shown in Fig. 5.15. For sample C, its curve extends in a straight-line as photon energy is below 3.0 eV, and changes it slope slightly at round 3.2 eV. However, for the other samples prepared at higher temperatures, inflection points could be clearly observed, especially for sample G. The dependence of band gaps on crystallization states, which has been introduced in Chapter 4, was verified in the CuO:In thin films with M ratio of 7%. The localized and defect states as mentioned in the Davis-Mott model could explain the relatively high absorptances below the inflection points of samples C, F, and G.

Quantum confinement has been found to cause blue shift or the broadening of band gap. The size dependency of the band gap of a semiconductor nano-particle, known as Brus theory [118], is given as follows:

$$E = E_g + \frac{\pi^2\hbar^2}{2m_o R^2}\left(\frac{1}{m_e^*} + \frac{1}{m_h^*}\right) - \frac{1.8e^2}{4\pi\varepsilon_o\varepsilon_\infty R} \tag{5.6}$$

R is the radius of the semiconductor particle, while E_g represents the band gap of the bulk semiconductor. The second term in the equation represents the particle-in-abox quantum localization energy and has a $1/R^2$ dependence. The third term represents the Coulomb energy with a 1/R dependence. In the limit of large R the value of E approaches that of E_g. Although the XRD patterns suggested nano-sized CuO grains in the films, we are certain that this model alone cannot explain the band gap broadening of the films as Brus theory is for single-phase materials.

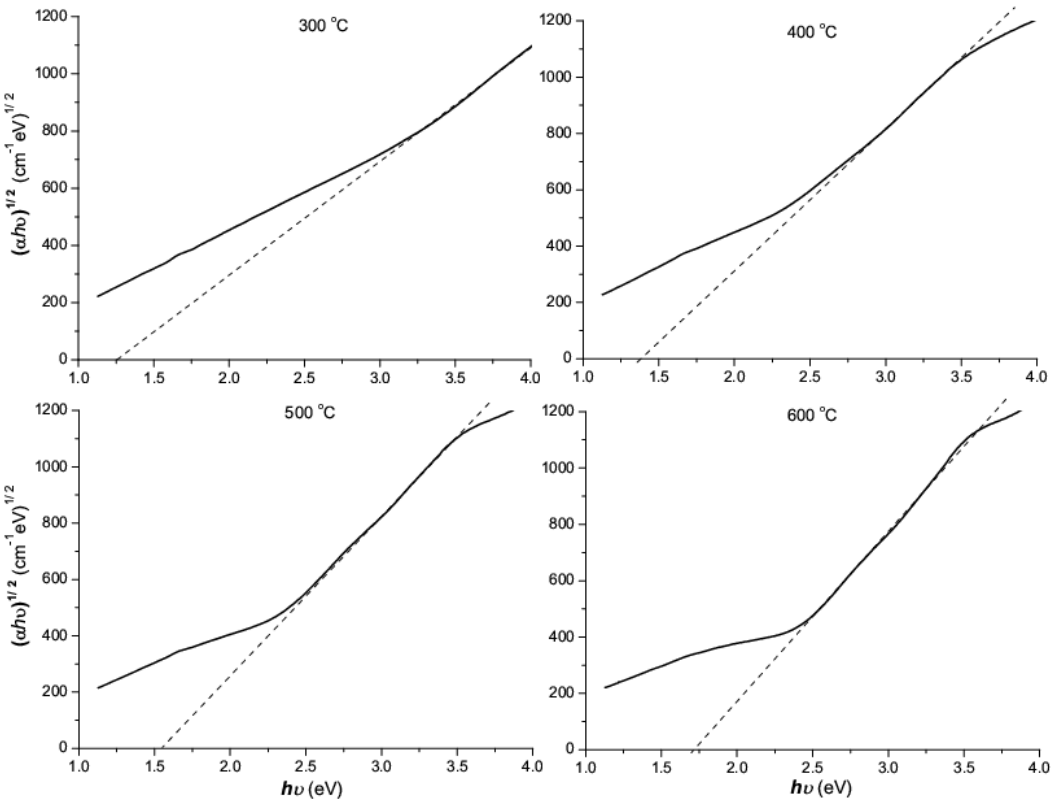

Figure 5.15: Photon energy ($h\nu$) dependence of $(\alpha h\nu)^{1/2}$, where α is absorption coefficient, h is Plank constant and ν is photon frequency, of CuO thin films deposited at different substrate temperatures: 300, 400, 500, and 600 °C.

Referring to the grain sizes of samples C, F and G (6.5±0.3, 7.3±0.3, and 7.0±0.3 nm, respectively), it is obvious that the quantum size effect itself cannot explain the increase of the optical band gaps because sample C does not have the minimum grain size. The dependence of band gaps on crystallization states as introduced in Chapter 4 reminds us that the amorphous phase in the films cannot be neglected. As the substrate temperature increased from 300 °C to 600 °C, the amorphous parts in the films might decreased and the influence of quantum size effect might be more and more obvious, therefore we could observe the highest optical band gap in sample G.

5.6 Summary

In this chapter, as the first report of indium incorporated CuO thin films, the influence of the various experimental parameters on the electrical and optical properties of CuO:In thin films was presented, especially of indium concentration and substrate temperature. The mechanism of the low resistivities of some films was discussed by the characterization technologies such as XRD, TEM, and XPS, etc.

Conductive CuO:In thin films prepared by PE-CVD method was achieved for the fist time as to our best knowledge. As the M ratios in the mixed precursors increased from 5% to 15%, the resistivities of the films prepared at 400 °C were 13.92, 7.35, 8.73, and 14.43 Ωcm, respectively, whose corresponding activation energies were 0.154, 0.140, 0.165, and 0.208 eV, respectively. The films having the M ratio of 0% and over 20% were almost insulating. Positive hole induced by the negatively charged defect complex $In_{Cu}^{\cdot}$ and $V_{Cu}^{''}$ was assumed to be the root cause of the low resistivities. XPS study excluded the possibility that the low resistivities came from a reduction of Cu(2+) to Cu(+). The increase of optical band gaps from 1.42 to 1.75 eV was reported, as the M ratios in the films increased from 0% to 25%. Orbital hybridization associated with indium ions and composition change were considered to be responsible for it. The significance of these findings lies in that it provided an approach to balance *p*-type CuO:In thin films' optical and electrical properties by changing the concentration of the incorporated indium atoms.

A new satellite feature, which has never been reported in CuO or Cu_2O, was found in XPS spectra of Cu $2p^{3/2}$ core level for all the films. Defect energy levels

associated with the indium doping were assumed to be related with the new shake-up structure. Further studying on their electronic structure needs to be conducted to investigate its root cause.

Based on the study of the films prepared by using the mixed precursors with the M ratio of 7%, a strong influence of the oxygen flow rate and substrate temperature on the films' properties was found. The resistivities of the films prepared at the oxygen flow rate of 15, 30, 45, and 60 sccm were 77.22, 57.72, 18.83, and 15.11 Ωcm, respectively. This dependence of resistivity on the oxygen pressure supported the formation reaction of positive hole due to incorporation of indium atom. The films deposited at the substrate temperature of 500 °C and 600 °C were almost insulating; meanwhile, the film at 300 °C showed a low resistivity, i.e. 8.82 Ωcm, which suggested that the nano-sized CuO grains were not the root cause of the low resistivities. The nonstoichiometry determined by the substrate temperature seemed play a more important role on it. The increase of optical band gap from 1.25 to 1.71 eV with the substrate temperature increasing from 300 to 600 °C was explained by the dependence of band gaps on crystallization states. The quantum size effect might contribute more to the broadening of the band gaps as amorphous parts in the films decreased with increasing the substrate temperature. The film structure and indium concentration were found to be the most critical parameters controlling the optical and electrical properties of the films.

Chapter 6

Summary and Future Work

6.1 Summary

A systematic investigation of copper indium oxide thin films prepared by PE-CVD using metal-organic precursors $Cu(acac)_2$ and $In(acac)_3$ was conducted in this project. Cu-In-O thin films deposited using the mixed precursors $Cu(acac)_2$ and $In(acac)_3$ with In/Cu atomic ratio of 1 under different substrate temperatures and atmospheres were investigated as the first part of this work. XRD results revealed a structural transition from amorphous state to nano-crystalline CuO and In_2O_3 phases as the substrate temperature increased from 400 to 700 °C. Overlapping of ns orbital of heavy metal cations having (n-1)d^{10}ns^0 electronic structure (Cu and In in our case) was assumed responsible for the amorphous structure at low substrate temperatures. No significant structural difference was found for two substrates, i.e. x-cut quartz and (100) silicon. The influence of oxygen flow rate and working

pressure on the structures of films deposited at substrate temperature of 600 °C was investigated and no strong dependence was found. The absence of $CuInO_2$ and $Cu_2In_2O_5$ phases in the films obtained under different preparation conditions might suggest that there was no solid state reaction occurred in the CVD process. All the films in this part were semi-transparent due to the d-d transitions in Cu^{2+} ions and insulating in nature, which indicated that existence of amorphous or crystalline In_2O_3 phase could make *p*-type conduction less possible.

The other main focus of this thesis was indium incorporated CuO thin films. An indium concentration dependence of structural, electrical and optical properties was observed for the films deposited at 400 °C, whose structures evolved from nano-crystalline characteristic to amorphous state as the M ratio increased from 0% to 25%. The lowest resistivity of 7.35 Ωcm was achieved, with the activation energy of 0.140 eV, for the film with In/Cu atomic ratio of 8.3%. Copper vacancy induced by the incorporation of indium atom was assumed to be the root cause of the low resistivity. XPS study excluded the possibility that the low resistivity came from a reduction of Cu(2+) to Cu(+). The increase of optical band gap with indium concentration was found as the M ratios in the films increased from 0% to 25%, which was explained by an wider 3*d*-sub-bands caused by the 3*d* orbital hybridization associated with indium ions in the form of Cu-O-In bonding. A new satellite feature was found in XPS spectra of Cu $2p^{3/2}$ core level for all the films. Defect energy levels associated with the indium doping were assumed to be related with it.

The effects of the substrate temperature and oxygen flow rate on resistivity were

investigated for the films prepared using the mix precursors with In/Cu atomic ratio of 7%. As the oxygen flow rate was raised from 50, 100, 150, to 200 sccm the resistivity of the films deposited at 400 °C decreased from 77.22±2.34, 57.72±3.05, 18.83±0.02, to 15.11±0.64 Ωcm, respectively. These results supported the formation reaction of copper vacancy induced by doping indium atoms and could be explained well in terms of chemical reaction equilibrium with respect to oxygen pressure. The substrate temperature strongly influenced both the film structure and the resistivity. The film deposited at 300 °C was amorphous with a resistivity of 8.82±0.35 Ωcm, which suggested that the small CuO grain size could not be the root cause of low resistivity and the nonstoichiometry in the amorphous matrix might decide the resistivity, in contrast to the prediction in literature. The resistivity of the films grown at 500 °C and 600 °C were almost insulating. In_2O_3 phase and texture orientation change were observed in the films. The dependence of band gaps on crystallization states caused the optical band gaps of the films increased from 1.25 to 1.71 eV with increasing the substrate temperature from 300 to 600 °C.

In essence, the significance of this project lies in two aspects:

1) PE-CVD technique was used for the first time to explore the Cu-In-O ternary system and an investigation of crystallographical characteristic of Cu-In-O thin films at different growth conditions was reported. From which, some useful experiences were achieved for future study of preparing *p*-type semiconductor oxides.

2) *P*-type conductive CuO:In thin films were reported for the first time. Positive hole induced by the negatively charged defect complex $In_{Cu}^{\cdot}$ and $V_{Cu}^{''}$ was assumed

to be the root cause of the low resistivites. Changing indium concentration was proved to be effective to control the optical and electrical properties of p-type CuO:In thin films.

6.2 Future Work

It would be ideal if indium doped CuO single crystal thin films can be prepared by molecular-beam epitaxy, which will help to understand the defects associated with indium atoms with the help of a detailed structure study. Theoretical study by computer simulation is also valuable and instructive to explain the experimental observations, for example, the change of lattice spacing caused by the indium doping, formation energies and energy levels of defects related to indium ions, and electrical structure and optical band gap, etc.

All the CuO:In films in this study were prepared at above 300 °C. Further decreasing substrate temperature was limited by the dependence of chemical reaction on substrate temperature. Experimental work at lower temperature can be possible on other preparation methods such as sputtering and pulsed laser deposition, which will further improve the understanding of the influence of film structure and indium concentration on electrical and optical properties.

Similar study on other ternary systems such as Cu-Ga-O and Cu-Sr-O by the method of PE-MOCVD may be worth to be developed in order to explore proper combinations of conductivity and band gap suitable for practical applications. Multicomponent oxides consisting of Cu, In, Ga, Cr, and Sr elements are also valuable to be developed for the purpose of obtaining lower resistivity and higher optical band gap *p*-type semiconductors.

Bibliography

[1] A.J. Freeman, K.R. Poeppelmeier, T.O. Mason, R.P.H. Chang, and T.J. marks. *MRS Bulletin*, 25:45–51, 2000.

[2] R.J. Cava anf J.M. Phillips, J. Kwo, G.A. Thomas, R.B. van Dover, S.A. Carter, J.J. Krajewski, W.F. Peck, Jr., J.H. Marshall, and D.H. Rapkine. *Appl. Phys. Lett.*, 64:2071–2072, 1994.

[3] J.M. Phillips, R.J. Cava, G.A. Thomas, S.A. Carter, J. Kwo, T. Siegrist, J.J. Krajewski, J.H. Marshall, W.F. Peck, Jr., and D.H. Rapkine. *Appl. Phys. Lett.*, 67:2246–2248, 1995.

[4] H. Kawazoe, M. Yasukawa, H. Hyodo, M. Kurita, H. Yanagi, and H. Hosono. *Nature*, 389:940–942, 1997.

[5] H. Gong, Y. Wang, and Y. Luo. *Appl. Phys. Lett.*, 76:3959–3961, 2000.

[6] A.N. Banerjee and K.K. Chattopadhyay. *Progress in Crystal Growth and Characterization of Materials*, 50:52–105, 2005.

[7] C.H. Ong and H. Gong. *Thin Solid films*, 445:299–303, 2003.

[8] T. Minami, K. Shimokawa, and T. Miyata. *J. Vac. Sci. Technol. A*, 16:1218–1221, 1998.

[9] J. Asbalter and A. Subrahmanyam. *J. Vac. Sci. Technol. A*, 18:1672–1676, 2000.

[10] E. Bobeico, F. Varsano, C. Minarini, and F. Roca. *Thin Solid Films*, 444:70–74, 2003.

[11] C. Millon, J.L. Deschanvres, C. Jiménez, N. Macsporran, B. Servet, O. Durand, and M. Modreanu. *Surface and Coatings Technology*, Article in Press, 2007.

[12] H. Yanagi, T. Hase, S. Ibuki, K. Ueda, and H. Hosono. *Appl. Phys. Lett.*, 78:1583–1585, 2001.

[13] M. Shimode, M. Sasaki, and K. Mukaida. *J. Solid State Chem.*, 151:16–20, 2000.

[14] J.E. Clayton, D.P. Cann, and N. Ashmore. *Thin Solid Films*, 411:140–147, 2002.

[15] E.J.W. Verwey, P.W. Haaijman, F.C. Romeijin, and G.W. Oosterhout. *Philips Res. Repts.*, 5:1734–1741, 1950.

[16] Y. Ohya, S. Ito, T. Ban, and Y. Takahashi. *Key Engi. Mate.*, 181-182:113–116, 2000.

[17] K. Suba, O.G. Singh, B.D. Padalia, Om. Prakash, and D. Chandrasekharam. *Mate. Res. Bull.*, 29:443–450, 1994.

[18] S. Suda, S. Fujitsu, K. Koumoto, and H. Yanagida. *Jpn. J. Appl. Phys.*, 31:2488–2491, 1992.

[19] F. Lanza, R. Feduzi, and J. Fuger. *J. Mater. Res.*, 5:1739–1742, 1990.

[20] H.O. Pierson. *Handbook of Chemical Vapor Deposition: Principles,Technologies and Applications*. William Andrew, Norwick, 1999.

[21] B.G. Lewis and D.C. Paine. *MRS Bulletin*, 20:20–26, 2000.

[22] K.L. Chopra, S. Major, and D.K. Pandya. *Thin Solid Films*, 102:1–46, 1983.

[23] I. Hamberg and C.G. Granqvist. *J. Appl. Phys.*, 60:123–160, 1986.

[24] R. Latz, K. Michael, and M. Scherer. *Jpn. J. Appl. Phys.*, 30:149–151, 1991.

[25] Y. Nakato, K.I.Kai, and K. Kawabe. *Sol. Energy Mater. Sol. Cells*, 37:323–335, 1995.

[26] B.H. Lee, I.G. Kim, S.W. Cho, and S.H. Lee. *Thin Solid Films*, 302:25–30, 1997.

[27] C.G. Granqvist, A. Azens, A. Hjelm, L. Kullman, G.A. Niklasson, D. R¨n-now, M. Veszelei M.S. Mattsson, and G. Vaivars. *Sol. Energy*, 63:199–216, 1998.

[28] R.G. Gordon. *MRS Bulletin*, 25:52–57, 2000.

[29] D. Adler and J. Feinleib. *Phys. Rev. B*, 2:3112–3134, 1970.

[30] H. Sato, T. Minami, S. Takata, and T. Yamada. *Thin Solid Films*, 236:27–31, 1995.

[31] E. Antolini. *J. Mater. Sci.*, 27:3335–3340, 1992.

[32] P. Lunkenheimer, A. Loidl, C. R. Ottermann, and K. Bange. *Phys. Rev. B*, 44:5927–5930, 1991.

[33] D.C. Look. *Mater. Sci. Engi. B*, 80:383–387, 2001.

[34] A.F. Kohan, G. Ceder, D. Morgan, and C.G. Van de Walle. *Phys. Rev. B*, 61:15019–15027, 2000.

[35] K. Minegishi, Y. Koiwai, Y. Kikuchi, K. Yano, M. Kasuga, and A. Shimizu. *Jpn. J. Appl. Phys.*, 36:L1453–L1455, 1997.

[36] T. Aoki, Y. Hatanaka, and D.C. Look. *Appl. Phys. Lett.*, 76:3257–3258, 200.

[37] K.k. Kim, H.S. Kim, D.K. Hwang, J.H. Lim, and S.J. Park. *Appl. Phys. Lett.*, 83:63–65, 2003.

[38] G.X. Hu, H. Gong, E.F. Chor, and P. Wu. *Appl. Phys. Lett.*, 89:251102, 2007.

[39] N. Duan, A.W. Sleight, M.K. Jayaraj, and J. Tate. *Appl. Phys. Lett.*, 77:1325–1326, 2000.

[40] J. Tate, M.K. Jayaraj, A.D. Draeseke, T. Ulbrich, A.W. Sleight, K.A. Vanaja, R. Nagarajan, J.F. Wager, and R. L. Hoffman. *Thin Solid Films*, 411:119–124, 2002.

[41] K. Ueda, T. Hase, H. Yanagi, H. Kawazoe, H. Hosono, H. Ohta, M. Orita, and M. Hirano. *J. Appl. Phys.*, 89:1790–1793, 2001.

[42] R. Nagarajan, N. Duan, M.K. Jayaraj, J. Li, K.A. Vanaja, A. Yokochi, A. Draeseke, J. Tate, and A.W. Sleight. 3:265–270, 2001.

[43] J. Asbalter and A. Subrahmanyam. *J. Vac. Sci. Technol. A*, 18:1672–1676, 2000.

[44] H. Katayama-Yoshida, T. Nishimatsu, T. Yamamoto, and N. Orita. *Phys. Status Solidi B*, 210:429–436, 1998.

[45] H.C. Kandpal and R. Seshadri. *Solid State Sci.*, 4:1045–1052, 2002.

[46] X.L. Nie, S.H. Wei, and S.B. Zhang. *Phys. Rev. Lett.*, 88:066405, 2002.

[47] Von G. Bergerhoff and H. Kasper. *Acta Cryst. B*, 24:388–391, 1968.

[48] T. Wada, T. Negami, and M. Nishitani. *Appl. Phys. Lett.*, 62:1943–1945, 1993.

[49] T. Wada, T. Negami, and M. Nishitani. *J. Mater. Res.*, 8:545–550, 1992.

[50] Li Liu. Towards a better understanding of the electrical properties of $CuInO_2$, a delafossite TCO. Master's thesis, NATIONAL UNIVERSITY OF SINGAPORE, 2004.

[51] H. Hahnn and C. Lorent. *Allg. Chem.*, 279:281–285, 1955.

[52] S. Park and D.A. Keszler. *J. Solid State Chem.*, 173:355–358, 2003.

[53] C.W. Teplin, T. Kaydanova, D.L. Young, J.D. Perkins, D.S. Ginley, A. Ode, and D.W. Readey. *Appl. Phys. Lett.*, 85:3789–3791, 2004.

[54] A.E. Rakshani. *Solid State Electron*, 29:7–17, 1986.

[55] J. Ghijsen, L.H. Tjeng, J. van Elp, H. Eskes, J. Westerink, G.A. Sawatzky, and M.T. Czyzyk. *Phys. Rev. B*, 38:11322–11330, 1988.

[56] B.P. Rai. *Solar Cells*, 25:265–272, 1988.

[57] S. Ishizuka, S. Kato, T. Maruyama, and Katsuhiro Akimoto. *Jpn. J. Appl. Phys.*, 40:2765–2768, 2001.

[58] A.O. Musa, T. Akomolafe, and M.J. Carter. *Sol. Energy Mater. Sol. Cells*, 51:305–316, 1998.

[59] D. Trivich, E.Y. Wang, and R.J. Komp. *13th IEEE Photovoltaic Specialists Conf. Washington DC, 1978*. IEEE, New York, 1978.

[60] S. Ishizuka, S. Kato, Y. Okamoto, and K. Akimoto. *Appl. Phys. Lett.*, 80:950–952, 2002.

[61] S.C. Ray. *Sol. Energy Mater. Sol. Cells*, 68:307–312, 2001.

[62] F. Marabelli, G.B. Parravicini, and F. Salghetti-Drioli. *Phys. Rev. B*, 52:1433–1436, 1995.

[63] B. Balamurugan and B.R. Mehta. *Thin Solid Films*, 396:90–96, 2001.

[64] D.X. Wu, Q.M. Zhang, and M. Tao. *Phys. Rev. B*, 73:235206, 2006.

[65] L.C. Wang, K. Han, and M. Tao. *J. Electrochem. Soc.*, 154:D91–D94, 2007.

[66] P. Samarasekara, M.A.K. Mallika Arachchi, A.S. Abeydeera, C.A.N. Fernando, A.S. Disanayake, and R.M.G. Rajapakse. *Bull. Mater. Sci.*, 28:483–487, 2005.

[67] S. Grugeon P. Poizot, S. Laruelle and J. M. Taracon. *Nature*, 407:496–499, 2000.

[68] A. Cruccolini, R. Narducci, and R. Palombari. *Sens. Actuat. B*, 98:227–232, 2005.

[69] R.V. Kumar, Y. Diamant, and A. Gedanken. *Chem. Mater.*, 12:2301–2305, 2000.

[70] S. Anandan, X.G. Wen, and S.H. Yang. *Mater. Chem. Phys.*, 93:35–40, 2005.

[71] H. Zhu, F. Zhao, L.Q. Pan, Y.P. Zhang, Ch.F. Fan, Y. Zhang, and J.Q. Xiao. *J. Appl. Phys.*, 101:09H111, 2007.

[72] G. Narsinga Rao, Y.D. Yao, and J.W. Chen. *J. Appl. Phys.*, 101:09H119, 2007.

[73] V.I. Anisimov, J. Zaanen, and O.K. Andersen. *Phys. Rev. B*, 44:943–954, 1991.

[74] V.I. Anisimov, F. Aryasetiawan, and A.I. Liechtenstein. *J. Phys.: Condens. Matter*, 9:767–808, 1997.

[75] H. Suhr, Ch. Oehr, H. Holzschuh, F. Schmaderer, G. Wahl, Th. Kruck, and A. Kinnen. *Phys. C*, 153:784–785, 1988.

[76] H. Holzschuh and H. Suhr. *Appl. Phys. A: Solid Surfaces*, 51:486–490, 1990.

[77] M.V. Jorge, R.O. Jorge, M.A.R. Victor, and R. Facundo. *Appl. Catal. A*, 238:1–9, 2003.

[78] T. Maruyama. *Jpn. J. Appl. Phys.*, 37:4099–4102, 1998.

[79] Y.S. Gong, C. Lee, and C.K. Yang. *J. Appl. Phys.*, 77:5422–5425, 1995.

[80] B. Orel, F. vegl, N. Bukovec, and M. Kosec. *J. Non-Cryst. Solids*, 159:49–64, 1993.

[81] A. Parretta, M.K. Jayaraj, A. Di Nocera, S. Loreti, L. Quercia, and A. Agati. *Phys. Status Solidi B*, 155:399–404, 1996.

[82] P. Samarasekara, N.T.R.N. Kumara, and N.U.S. Yapa. *J. Phys.: Condens. Matter*, 18:2417–2420, 2006.

[83] T. Itoha and K. Maki. *Vacuum*, 81:1068–1076, 2007.

[84] R. Widmer, F.J. Haug, P. Ruffieux, O. Groning, M. Bielmann, P. Groning, and R.J. Fasel. *J. Am. Chem. Soc.*, 128:14103–14108, 2006.

[85] R.E. Leuchter and L.S. Hristakos. *Mater. Res. Soc. Symp. Proc.*, 401:551–556, 1996.

[86] R. Boucher. *J. Phys. Chem. Solids*, 66:1234–1239, 2005.

[87] D.H. Yoon, J.H. Yu, and G.M. Choi. *Sens. Actuat. B*, 46:15–23, 1998.

[88] J.L. Vossen and W. Kern. *Thin Films Processes II.* Academic Press, Boston, 1991.

[89] C. Kittel. *Introduction to Solid State Physics.* John Wiley Sons, New York, 7 edition, 1996.

[90] B.D. Cullity. *Elements of X-ray Diffraction.* Addison-Wesley, Boston, two edition, 1978.

[91] J.F. Moulder, W.F. Stickle, P.E. Sobol, and K.D. Bomben. *Handbook of X-ray Photoelectron Spectroscopy*. Perkin-Elmer, Eden Prairie, 1992.

[92] J.W. Mayer and S.S. Lau. *Electron Materials Science: for Integrated Circuits in Si and GaAs*. Macmillan, New York, 1990.

[93] P.Y. Yu and M. Cardona. *Foundamentals of Semiconductors: Physics and Materials Properties*. Springer-Verlag, Berlin, 1996.

[94] H.L. Hartnagel, A.L. Dawar, A.K Jain, and C. Jagadish. *Semiconducting Transparent Thin Films*. Institute of Physics, Bristol and Philadelphia, 1995.

[95] H. Hosono, N. Kikuchi, N. Ueda, and H. Kawazoe. *J. Non-Cryst. Solids*, 198-200:165–169, 1996.

[96] J. Robertson. *J. Phys. C*, 12:4767–4776, 1979.

[97] M. Sorescu, L. Diamandescu, D. Tarabasanu-Mihaila, and V.S. Teodorescu. *J. Mater. Sci.*, 39:675–677, 2004.

[98] I. Costina and R. Franchy. *Appl. Phys. Lett.*, 78:4139–4141, 2001.

[99] J.L. Cai and H. Gong. *J. Appl. Phys.*, 98:033707, 2005.

[100] V.R. Katti, A.K. Debnath, K.P. Muthe, Manmeet Kaur, A.K. Dua, S.C. Gadkari, S.K. Gupta, and V.C. Sahni. *Sens. Actuators B*, 96:245–252, 2003.

[101] K.K. Baek and H.L. Tuller. *Sens. Actuators B*, 13:238–240, 1993.

[102] Y.K. Jeong and G.M. Choi. *J. Phys. Chem. Solids*, 57:81–84, 1996.

[103] H. Okamoto, K. Hattori, and Y. Hamakawa. *J. Non-Cryst. Solids*, 164-166:445–448, 1993.

[104] J. Singh. *J. Mater. Sci.: Mater. Electro.*, 14:689–692, 2003.

[105] P.A. Cox. Clarendon Press, London, 1992.

[106] S. Asada and S. Sugano. *J. Phys. Soc. Jpn.*, 41:1291–1299, 1976.

[107] S. Larsson. *Chem. Phys. Lett.*, 32:401–406, 1975.

[108] S. Larsson. *Chem. Phys. Lett.*, 40:362–366, 1976.

[109] R. Zimmermann, P. Steiner, R. Claessen, F. Reinert, S. Hüfnert, P. Blaha, and P. Dufek. *J. Phys.: Condens. Matter*, 11:1657–1682, 1999.

[110] S. Narushima, H. Mizoguchi, K. i. Shimizu, K. Ueda, H. Ohta, M. Hirano, T. Kamiya, and H. Hosono. *Adv. Mater.*, 15:1409–1413, 2003.

[111] C.C. Chusuei, M.A. Brookshier, and D.W. Doodman. *Langmuri*, 15:2806, 1999.

[112] C.R. Brundle and A.D. Baker. *Electron Spectroscopy: Theory, Techniques and Applications.* Academic Press, New York, 2 edition, 1978.

[113] T. Novakov. *Phys. Rev. B*, 3:2693–2698, 1971.

[114] G. van der Laan, C. Westra, C. Haas, and G.A. Sawatzky. *Phys. Rev. B*, 23:4369–4380, 1981.

[115] M. Scrocco. *Chem. Phys. Lett.*, 63:52–56, 1979.

[116] L. Yin, I. Adler, T. Tsang, L.J. Matienzo, and S.O. Grim. *Chem. Phys. Lett.*, 24:81–84, 1974.

[117] C.B. Azzoni, G.B. Parravicini, G. Samogia, P. Ferloni, and F. Parmigiani. *Z. Naturforsch*, 45a:790–794, 1990.

[118] L.E. Brus. *J. Chem. Phys.*, 80:4403–4409, 1984.